Reynolds-stress Budgets in an Impinging Shock Wave/Boundary-layer Interaction

Manan A. Vyas* and Dennis A. Yoder†
NASA Glenn Research Center, Cleveland, Ohio, 44135, USA
Datta V. Gaitonde‡
The Ohio State University, Columbus, Ohio, 43210, USA

Implicit large-eddy simulation (ILES) of a shock wave/boundary-layer interaction (SBLI) was performed. Comparisons with experimental data showed a sensitivity of the current prediction to the modeling of the sidewalls. This was found to be common among various computational studies in the literature where periodic boundary conditions were used in the spanwise direction, as was the case in the present work. Thus, although the experiment was quasi-two-dimensional, the present simulation was determined to be two-dimensional. Quantities present in the exact equation of the Reynolds-stress transport, i.e., production, molecular diffusion, turbulent transport, pressure diffusion, pressure strain, dissipation, and turbulent mass flux were calculated. Reynolds-stress budgets were compared with past large-eddy simulation and direct numerical simulation datasets in the undisturbed portion of the turbulent boundary layer to validate the current approach. The budgets in SBLI showed the growth in the production term for the primary normal stress and energy transfer mechanism was led by the pressure strain term in the secondary normal stresses. The pressure diffusion term, commonly assumed as negligible by turbulence model developers, was shown to be small but non-zero in the normal stress budgets, however it played a key role in the primary shear stress budget.

Nomenclature

δ_{99}	boundary-layer thickness
δ_{ij}	Kronecker delta
ϵ	isotropic dissipation
ϵ_{ij}	dissipation tensor
γ	specific heat ratio
κ	thermal conductivity constant or Kármán constant
$\mathbf{F}$, $\mathbf{G}$, $\mathbf{H}$	flux vectors
$\mathbf{S}$	source vector
$\mathbf{U}$	solution vector
$\mathcal{D}^{\nu}_{ij}$	molecular diffusion tensor
$\mathcal{D}^{P}_{ij}$	pressure diffusion tensor
$\mathcal{D}^{T}_{ij}$	turbulent diffusion tensor
$\mathcal{D}_{ij}$	diffusion tensor (total)
$\mathcal{M}_{ij}$	turbulent mass flux tensor
$\mathcal{P}_{ij}$	production tensor
μ	molecular viscosity
Π_{ij}	pressure strain tensor

*Aerospace Engineer, Inlets and Nozzles Branch, 21000 Brookpark Road, and AIAA Member.
†Aerospace Engineer, Inlets and Nozzles Branch, 21000 Brookpark Road, and AIAA Associate Fellow. ‡John Glenn Chair Professor, Department of Mechanical and Aerospace Engineering, and AIAA Fellow.

ρ	density
τ_{ij}	Reynolds-stress tensor
θ	boundary-layer momentum thickness
ζ	second viscosity
B	law of the wall intercept constant
C_p	specific heat at constant pressure
e	internal energy
e_0	total energy
I_x, I_y, I_z	digital filter length scale in x, y, and z directions, respectively
k	turbulent kinetic energy
L	length scale
M	Mach number
N_y, N_z	digital filter size in y and z directions
p	pressure
Pr	Prandtl number
Re	Reynolds number
s	span
S_{ij}	mean strain-rate tensor
s_{ij}	instantaneous strain-rate tensor
T	temperature
t	time
t_{ij}, $\boldsymbol{t}$	viscous stress tensor
u, v, w	non-dimensional velocity in x, y, and z directions, respectively
V	velocity magnitude
x, y, z	non-dimensional coordinates

Subscripts

0	total condition
i, j, k	index notation, equal to 1, 2, or 3
imp	impingement location
int	interaction
inv	inviscid
ref, ∞	reference value same as freestream value
sep	separation
vis	viscous
w	wall

Conventions

$\bar{}$	Reynolds averaged
$\tilde{}$	Favre averaged

Superscripts

$'$	Reynolds decomposition
$''$	Favre decomposition
$*$	non-dimensional value
T	transpose
tot	total
tr	trace

I. Introduction

Literature is replete with experimental, numerical, and modeling studies of shock wave/boundary-layer interactions (SBLIs).[1–3] This interest is warranted because SBLIs are ubiquitous in transonic, supersonic, and hypersonic speed regimes and thus relevant to commercial, military, and space vehicles of the past, present, and future. SBLIs are known to create excessive unsteady aerothermal loads that can compromise structural integrity, cause component failure, and result in loss of control. In particular and of relevance to the

present work is the adverse pressure gradient in the propulsion flowpath, which can cause flow separation, distortion, and loss in engine efficiency. Because of this, SBLIs are one of the most actively researched phenomena in high speed flows, yet far from being completely understood, and hence numerical simulation and modeling of SBLIs are a continuing challenge.

The unsteady nature of SBLIs and the resulting three-dimensional (3D) separation, often including corner separation (i.e., propulsion flowpaths are often rectangular), make their prediction extremely difficult. Investigating the source of low-frequency unsteadiness of the reflected (or separation) shock in an SBLI, which is typically one or two orders of magnitude lower than the frequencies within the incoming turbulent boundary layer,[1,4,5] is important for flow control strategies. However, understanding the locally anisotropic and inhomogeneous turbulence field is key to accurate prediction of separation via numerical simulations and modeling of SBLIs.

While the corner influence is not inherent to the incident/reflected shock configuration, it is present in practical situations where sidewalls exist, e.g. wind tunnels, inlets, isolators, etc. Also, it is important to address the fact that the majority of experimental configurations involving compression ramp and incident/reflected shock exhibit some level of corner influence due to corner separation, which renders portions of the flow near corners 3D, while the centerline remains two-dimensional (2D). Due to such a prevalence and coupling, corner influence has become an area of active research as shown by the works of Babinsky et al.,[6] Benek et al.,[7,8] and Eagle at al.,[9] which includes experimental as well as numerical investigations.

An elementary understanding of separation and corner influence exists, however modeling improvements from such understanding has yet to be realized. It is this uncertainty in the knowledge of SBLI physics which make them extremely difficult to model and simulate. An example of a canonical two-dimensional (2D) SBLI flowfield is shown in figure 1, where an incident oblique shock impinges on a turbulent boundary layer. Depending on the strength of the incident shock, the flow may not separate, incipiently separate, or completely separate. In figure 1, the flow is shown to separate. The streamwise length of the separation bubble is L_{sep}. The interaction length obtained by extending the inviscid portions of the incident and reflected shocks to the wall is L_{int}. The development of the separation results in the forward migration of the reflected shock, of course this is in a steady sense. In reality, the separation bubble has been shown to shrink and grow in size, which causes the reflected shock to oscillate aft (small separation) and forward (large separation) with a characteristic low frequency. Numerous experimental and computational works have shown this to be between Strouhal number $0.02 - 0.05$.[10]

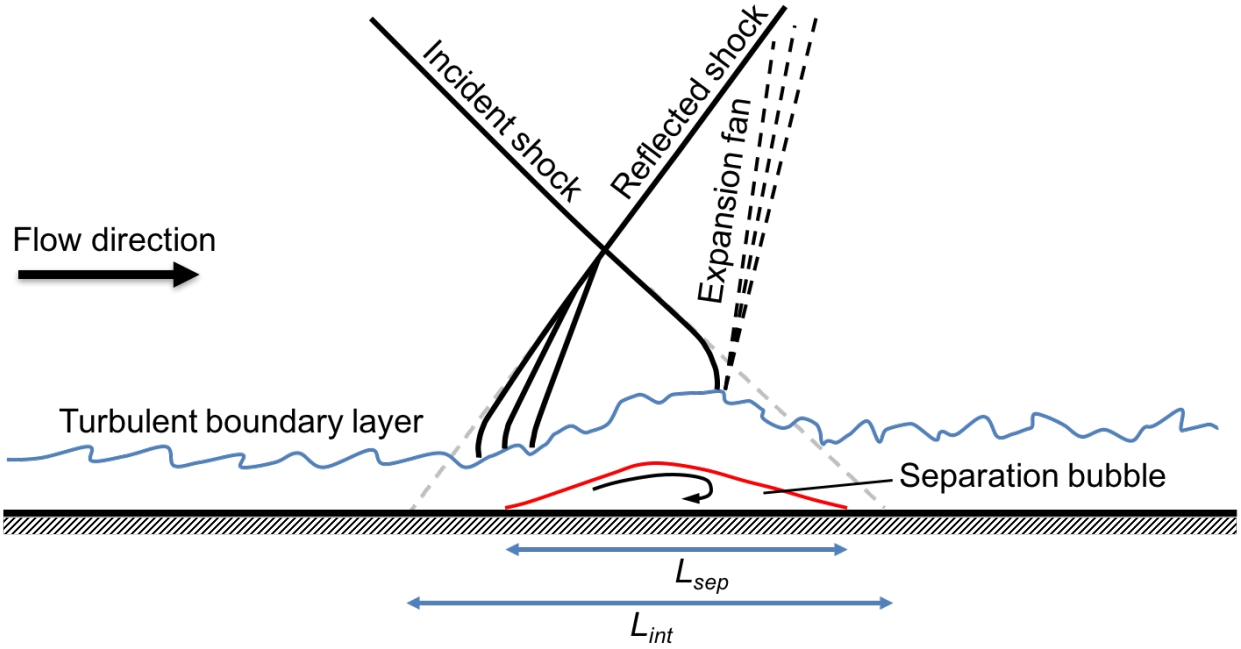

Figure 1. Two-dimensional anatomy of an impinging shock wave/boundary-layer interaction.

In most practical applications, Reynolds-averaged Navier-Stokes (RANS) computational fluid dynamics (CFD) solvers coupled with turbulence models are used to calculate flowfields where SBLIs are present. This is mainly due to their ease of use, and also because of the challenges presented by scale-resolving methods like hybrid RANS/large-eddy simulations (LES), LES, and direct numerical simulations (DNS) in the form of available computer resources and lengthy simulation times. However, scale-resolving methods offer significant gains in accuracy.

A list of scale-resolving approaches is compiled by Georgiadis et al.[11] in a paper that provides a summary of current practices in LES. In LES, large-scale structures are resolved and a sub-grid scale model is employed to model the scales which cannot be resolved by the mesh. A subset of LES is implicit LES (ILES). Like LES, ILES calculates the large-scale turbulent structures, but it does not explicitly model the smallest scales. Instead it uses a high-order low-pass Padé-type filter to dissipate energy in the high spatial wavenumber range.[12,13] So, the use of an explicit sub-grid scale model is completely avoided. Thus, ILES is an attractive approach for this work as it is not as expensive as DNS, but does provide a seamless changeover to DNS as the mesh resolution is refined.

A workshop was organized in 2011 by the American Institute of Aeronautics and Astronautics (AIAA) with an intent to share, assess, and determine the most promising SBLI prediction methods. The results obtained by the participants were compiled by DeBonis et al.[14] in which comparisons with experimental data and error metrics were presented. While the majority of solutions were obtained with RANS methods, some were obtained with hybrid RANS/LES, LES, and DNS. It was concluded that *the turbulence model played a significant role in variations among different RANS solutions* and *the error in all solutions increased as the adverse pressure gradient becomes stronger and the size of the separation increased.* It was also found that the scale-resolving methods provided some of the best and the worst solutions, clearly indicating that scale-resolving methods are feasible and accurate but that more development is needed.

Perhaps the most interesting revelation DeBonis et al.[14] presented was the fact that the relative accuracy of a method was not consistent for different variables of interest within the same solution, i.e. high prediction accuracy in $\bar{u}$ velocity did not guarantee the same accuracy for $\bar{v}$ velocity. This, combined with the other observations above, shows shortfalls of the current one- and two-equation turbulence models. Common among most turbulence models in use today is the Boussinesq eddy-viscosity approximation, which establishes a linear relation between the Reynolds-stress tensor, τ_{ij}, and the mean strain-rate tensor, S_{ij}. Such a relationship does not exist in shock-separated flows such as SBLI, flows where rapid changes in mean strain-rate occur, and where secondary flows are present—all examples of flows which are inhomogeneous and anisotropic.

Some efforts have been made to incorporate the above effects into existing turbulence models by modifying the turbulent kinetic energy, k, and dissipation rate, ϵ, equations to account for inhomogeneity and anisotropy. Hamlington and Dahm[15] addressed this by replacing the mean strain-rate tensor in a standard two-equation approach with a new mean strain-rate tensor that accounts for flow history, thus allowing the Reynolds-stress tensor to adjust over a finite lag while retaining the simplicity of a two-equation formulation. Sinha et al.[16] included additional terms representing shock unsteadiness in the k and ϵ equations. A linear analysis was used to model the unsteadiness in the $k-\epsilon$ model by realizing that a positive fluctuation in the streamwise velocity leads to the reflected/separation shock motion downstream, while a negative fluctuation in the streamwise velocity causes the reflected/separation shock to move upstream. Numerous other improvements have been suggested to the one- and two-equation turbulence model formulations, though discussing them is beyond the scope of this paper. Another approach is to completely bypass the linear relationship between the Reynolds-stress tensor and the mean strain-rate tensor in one- and two-equation formulations for nonlinear constitutive relations. In some of the more advanced techniques, a direct prescription of the Reynolds-stress tensor is sought using a nonlinear algebraic equation or by using a Reynolds-stress transport model. However, among these approaches, none has emerged as clearly superior.

In the authors' previous work, terms in the exact equation of turbulent kinetic energy were studied for a developing turbulent boundary layer and an SBLI.[17] However, due to increased interest in Reynolds-stress models, here the focus is shifted on the exact equation of Reynolds stress transport. Understanding of the various terms in the exact equation and their interactions with each other would shed light on the fundamental mechanisms present in SBLI. This knowledge may be used to improve the current turbulence models and/or propose new models. In the past, such efforts involved DNS studies of turbulent boundary layers,[18] channel flows,[19] and square ducts.[20] The present work is the first comprehensive examination of the Reynolds-stress transport terms within an SBLI flowfield. Our objective is twofold:

- Validate the simulation with an SBLI experimental database to ensure consistency of the computed quantities.
- Study the budgets of Reynolds stress and other relevant turbulence quantities with an intent to inform future model development.

II. Governing Equations

In this section the Reynolds stress transport equation will be discussed along with the equations pertinent to the ILES formulation and the digital filter approach, which is used to obtain turbulent fluctuations at the inflow.

A. Reynolds-stress Budget

The Reynolds stress is defined as

$$\bar{\rho}\tau_{ij} = -\overline{\rho u_i'' u_j''} \tag{1}$$

The Reynolds stress transport is given by equation 2. The first term on the left-hand side represents the unsteady term, while the second term represents the convection—together, the left-hand side is the substantial derivative. The budget terms are on the right-hand side.

$$\frac{\partial}{\partial t}(\overline{\rho u_i'' u_j''}) + \frac{\partial}{\partial x_k}(\overline{\rho u_i'' u_j''}\tilde{u}_k) = \mathcal{P}_{ij} + \mathcal{D}_{ij} - \bar{\rho}\epsilon_{ij} + \Pi_{ij} + \mathcal{M}_{ij} \tag{2}$$

Each term on the right-hand side of equation 2 is defined as

$$\mathcal{P}_{ij} = -\overline{\rho u_i'' u_k''}\frac{\partial \tilde{u}_j}{\partial x_k} - \overline{\rho u_j'' u_k''}\frac{\partial \tilde{u}_i}{\partial x_k} \qquad \text{Production} \tag{3}$$

$$\mathcal{D}_{ij} = \mathcal{D}_{ij}^{\nu} + \mathcal{D}_{ij}^{T} + \mathcal{D}_{ij}^{P} \qquad \text{Diffusion} \tag{4}$$

$$\mathcal{D}_{ij}^{\nu} = \frac{\partial}{\partial x_k}\left[\overline{u_i'' t_{kj} + u_j'' t_{ki}}\right] \qquad \text{Molecular Diffusion} \tag{5}$$

$$\mathcal{D}_{ij}^{T} = -\frac{\partial}{\partial x_k}\left[\overline{\rho u_i'' u_j'' u_k''}\right] \qquad \text{Turbulent Diffusion} \tag{6}$$

$$\mathcal{D}_{ij}^{P} = -\frac{\partial}{\partial x_k}\left[\overline{p' u_i''}\delta_{jk} + \overline{p' u_j''}\delta_{ik}\right] \qquad \text{Pressure Diffusion} \tag{7}$$

$$\Pi_{ij} = \overline{p'\left(\frac{\partial u_i''}{\partial x_j} + \frac{\partial u_j''}{\partial x_i}\right)} \qquad \text{Pressure Strain} \tag{8}$$

$$\bar{\rho}\epsilon_{ij} = \overline{t_{ki}\frac{\partial u_j''}{\partial x_k}} + \overline{t_{kj}\frac{\partial u_i''}{\partial x_k}} \qquad \text{Dissipation} \tag{9}$$

$$\mathcal{M}_{ij} = \overline{u_i''}\left(\frac{\partial \bar{t}_{kj}}{\partial x_k} - \frac{\partial \bar{p}}{\partial x_j}\right) + \overline{u_j''}\left(\frac{\partial \bar{t}_{ki}}{\partial x_k} - \frac{\partial \bar{p}}{\partial x_i}\right) \qquad \text{Mass Flux} \tag{10}$$

Here t_{ij} is the viscous stress tensor based on the instantaneous strain-rate tensor s_{ij}, and δ_{ij} is the Kronecker delta.

$$t_{ij} = 2\mu s_{ij} + \zeta\frac{\partial u_k}{\partial x_k}\delta_{ij} \tag{11}$$

In equation 11, ζ is obtained by relating it to μ. Such an assumption is valid for monatomic gases and widely used in computational fluid dynamics.

$$\zeta = -\frac{2}{3}\mu \tag{12}$$

B. Compressible Navier-Stokes Equations

The compressible Navier-Stokes equations in non-dimensional form are given by

$$\frac{\partial \rho}{\partial t} + \frac{\partial}{\partial x_i}(\rho u_i) = 0 \tag{13}$$

$$\frac{\partial}{\partial t}(\rho u_i) + \frac{\partial}{\partial x_j}(\rho u_i u_j + p\delta_{ij} - \frac{1}{Re} t_{ij}) = 0 \tag{14}$$

$$\frac{\partial}{\partial t}(\rho e_0) + \frac{\partial}{\partial x_i}\left[u_i(\rho e_0 + p) - \frac{1}{Re}(u_i t_{ij}) + \frac{1}{(\gamma-1)PrM^2Re} q_i\right] = 0 \tag{15}$$

The total energy and heat flux are defined as

$$e_0 = e + \frac{1}{2} u_i u_i \qquad\qquad q_i = -\mu \frac{\partial T}{\partial x_i} \tag{16}$$

The non-dimensionalization is performed using the following definitions where * (asterisk) represents non-dimensional quantities. Except equations 17a and 17b, the * has been dropped for simplicity and all quantities are non-dimensional in this paper, unless stated otherwise.

$$x_i^* = \frac{x_i}{L} \qquad u_i^* = \frac{u_i}{V_{ref}} \qquad t^* = \frac{t V_{ref}}{L} \qquad \rho^* = \frac{\rho}{\rho_{ref}} \tag{17a}$$

$$p^* = \frac{p}{\rho_{ref} V_{ref}^2} \qquad T^* = \frac{T}{T_{ref}} \qquad \mu^* = \frac{\mu}{\mu_{ref}} \qquad e^* = \frac{e}{V_{ref}^2} \tag{17b}$$

The reference conditions are the upstream freestream conditions and the length scale, L, is the same as the boundary-layer thickness, both are discussed later in section III.B. The non-dimensional parameters Reynolds number, Prandtl number, and Mach number are defined below. The specific heat at constant pressure is C_p and κ_{ref} is the thermal conductivity constant. The molecular viscosity, μ_{ref}, is calculated using Sutherland's law and a perfect gas is assumed.

$$Re = \frac{\rho_{ref} V_{ref} L}{\mu_{ref}} \qquad Pr = \frac{\mu_{ref} C_p}{\kappa_{ref}} \qquad M = \frac{V_{ref}}{\sqrt{\frac{\gamma p_{ref}}{\rho_{ref}}}} \tag{18}$$

The above Navier-Stokes equations can be expressed in flux-vector form as

$$\frac{\partial \mathbf{U}}{\partial t} + \frac{\partial \mathbf{F}_{inv}}{\partial x} + \frac{\partial \mathbf{G}_{inv}}{\partial y} + \frac{\partial \mathbf{H}_{inv}}{\partial z} = \frac{\partial \mathbf{F}_{vis}}{\partial x} + \frac{\partial \mathbf{G}_{vis}}{\partial y} + \frac{\partial \mathbf{H}_{vis}}{\partial z} + \mathbf{S} \tag{19}$$

where $\mathbf{U}$ is the solution vector defined as $\mathbf{U} = [\rho, \rho u, \rho v, \rho w, \rho e_0]^T$. The inviscid and viscous flux vectors are defined as

$$\mathbf{F}_{inv} = \begin{bmatrix} \rho u \\ \rho u + p \\ \rho uv \\ \rho uw \\ (\rho e_0 + p)u \end{bmatrix} \qquad \mathbf{F}_{vis} = \frac{1}{Re} \begin{bmatrix} 0 \\ t_{xx} \\ t_{xy} \\ t_{xz} \\ (ut_{xx} + vt_{xy} + wt_{xz}) + \frac{\mu}{(\gamma-1)PrM^2} \frac{\partial T}{\partial x} \end{bmatrix} \tag{20}$$

The above equations are transformed into curvilinear coordinates, and using the strong conservation form the following is obtained[21,22]

$$\frac{\partial \hat{\mathbf{U}}}{\partial t} + \frac{\partial \hat{\mathbf{F}}_{inv}}{\partial \xi} + \frac{\partial \hat{\mathbf{G}}_{inv}}{\partial \eta} + \frac{\partial \hat{\mathbf{H}}_{inv}}{\partial \zeta} = \frac{\partial \hat{\mathbf{F}}_{vis}}{\partial \xi} + \frac{\partial \hat{\mathbf{G}}_{vis}}{\partial \eta} + \frac{\partial \hat{\mathbf{H}}_{vis}}{\partial \zeta} + \hat{\mathbf{S}} \tag{21}$$

such that $\hat{\mathbf{U}} = \mathbf{U}/\mathbf{J}$ and $\hat{\mathbf{S}} = \mathbf{S}/\mathbf{J}$ where $\mathbf{J}$ represents the Jacobian of the transformation. The transformed flux vectors are defined as

$$\hat{\mathbf{F}}_{inv} = \frac{1}{\mathbf{J}}(\xi_x \mathbf{F}_{inv} + \xi_y \mathbf{G}_{inv} + \xi_z \mathbf{H}_{inv}) \tag{22}$$

$$\hat{\mathbf{F}}_{vis} = \frac{1}{\mathbf{J}}(\xi_x \mathbf{F}_{vis} + \xi_y \mathbf{G}_{vis} + \xi_z \mathbf{H}_{vis}) \tag{23}$$

and similarly $\hat{\mathbf{G}}_{inv}$, $\hat{\mathbf{H}}_{inv}$, $\hat{\mathbf{G}}_{vis}$, and $\hat{\mathbf{H}}_{vis}$.

C. Unsteady Inflow Boundary Method

In a previous study, budget of turbulent kinetic energy was investigated by Vyas et al.[17] using a similar approach to that taken here. However, in that work, the generation of the supersonic turbulent boundary layer was achieved by using the counterflow force model.[23–25] The approach, although functional, required a large streamwise domain to facilitate a transition from the specified laminar boundary-layer inflow profile to a turbulent boundary layer. Thus, an alternate approach where such laminar-to-turbulent transition can be avoided by specifying an unsteady boundary-layer profile at the inflow is highly desired. This will also allow for smaller mesh sizes or possibly transferring some of the mesh points into the area of interest, i.e., the shock wave/boundary-layer interaction region.

1. *The Digital Filter Approach*

The digital filter approach was originally proposed by Klein et al.,[26] where the filtering operation was performed in 3D space. Later, Veloudis et al.[27] investigated specification of varying filter coefficients in the wall-normal direction to allow for varying length scales. Xie and Castro[28] simplified and sped up the approach by performing the filtering operation on the 2D inflow plane and correlating the calculated 2D field with the one at the previous timestep to account for the length scale in streamwise direction using Taylor's hypothesis.[29] The approach was further improved by Touber and Sandham[30] and the current work closely follows their implementation of the digital filter.

Assume a set of p random numbers, $\{r_k\}_{1 \le k \le p}$, such that the set has zero mean and unit variance.

$$\overline{r}_k = \sum_{k=1}^{p} r_k/p = 0 \qquad\qquad \overline{r_k r_k} = \sum_{k=1}^{p} r_k^2/p = 1 \tag{24}$$

A filter operator can be defined, where N is a positive integer related to the filter length scale and $\{b_j\}_{-N \le j \le N}$, a set of real numbers, are the filter coefficients.

$$v_k \equiv F_N(r_k) = \sum_{j=-N}^{N} b_j r_{k+j} \tag{25}$$

The filter operator, equation 25, is linear and non-recursive. Thus the averaging and filtering operations commute, and knowing the properties of $\{r_k\}$ in equation 24, the following is true.

$$\overline{r}_k = 0 \qquad\qquad \overline{r_k r_{k+q}} = \sum_{j=-N+q}^{N} b_j b_{j-q} \tag{26}$$

Following the approach of Xie and Castro[28] and Touber and Sandham,[30] the correlation function was chosen to be exponential as opposed to Gaussian, assumed by Klein et al.[26] in the original work. Xie and Castro[28] argued that the choice of exponential form will produce an energy-decay rate in the inertial subrange which corresponds to slope of -2, rather than $-5/3$. However, the behavior of large-scale structures is realistically modelled. Such an assumption is valid since the digital filter is operational at the inflow plane

and the domain has enough length upstream of the region of interest to allow the flow to recover the correct velocity spectra in the inertial subrange. The two-point correlation at the $y-z$ inflow plane is defined as:

$$R(r,\alpha,t) = \exp\left(-\frac{\pi r}{2I}\right) \tag{27}$$

In equation 27, r is the separation variable, $\alpha = y = z = 0$, $t = 0$ is the time, and I is the length scale defined such that $I_\alpha = n_{I_\alpha}\Delta\alpha$. So equation 28 follows such that $q\Delta\alpha$ represents separation distance and q is the interval step.

$$R_{vv}(q\Delta\alpha) = \frac{\overline{v_k v_{k+q}}}{\overline{v_k v_k}} = \exp\left(-\frac{\pi|q|}{2n}\right) \tag{28}$$

Using equations 26 and 28, filter coefficients can be computed by solving:

$$\frac{\sum_{j=-N+q}^{N} b_j b_{j-q}}{\sum_{j=-N}^{N} b_j^2} = \exp\left(-\frac{\pi|q|}{2n}\right) \tag{29}$$

Xie and Castro[28] obtained a solution for filter coefficient b_k as:

$$b_k = \frac{\tilde{b}_k}{\left(\sum_{j=-N}^{N} \tilde{b}_j^2\right)^{(1/2)}} \text{ , where } \tilde{b}_k \simeq \exp\left(-\frac{\pi|k|}{n}\right) \tag{30}$$

In the above, N is defined as $N_\alpha \geq 2n_\alpha$. Thus, the above one-dimensional approach can be extended to calculate a 2D filter coefficient at the $y-z$ inflow plane as:

$$b_{jk} = b_j b_k \tag{31}$$

Thus, an approximation for a 2D filter coefficient becomes:

$$b_{jk} = \frac{\exp\left[-\pi\left(\frac{|j|}{n_y}+\frac{|k|}{n_z}\right)\right]}{\left\{\sum_{k=-N_z}^{N_z}\sum_{j=-N_y}^{N_y}\exp\left[-2\pi\left(\frac{|j|}{n_y}+\frac{|k|}{n_z}\right)\right]\right\}^{1/2}} \tag{32}$$

In general, the following steps are taken within the digital filter algorithm:

1. Generate a set of p random numbers with zero mean and unit variance corresponding to the 2D inflow mesh. Here, the Box-Muller theorem is used to combine two independent and uniformly distributed sets of numbers a and b in the range $(0,1)$ into c and d, which are independent and normally distributed, and also satisfy zero mean and unit variance conditions. They can be calculated as below, however, either one can be used.

$$c = \sqrt{-2\ln(a)}\cos(2\pi b) \qquad\qquad d = \sqrt{-2\ln(a)}\sin(2\pi b) \tag{33}$$

2. Select the relevant length scales, I_x, I_y, and I_z. Since the current implementation is 2D, I_y and I_z are converted into an equivalent number of grid points using the grid spacing, i.e., $n_{I_\alpha} = I_\alpha/\Delta\alpha$.

3. Now the filter coefficients can be calculated using equation 32. Filter bounds are calculated using $N_\alpha = 2n_{I_\alpha}$.

4. The filter coefficients calculated in equation 32 can now be used to filter the zero mean and unit variance normally distributed random numbers calculated in equation 33. Thus, we impose relevant $y-z$ length scales on the field of these normally distributed random numbers using equation 25.

5. The length scale in the x direction is imposed by correlating the old time step $(t-\Delta t)$ to the current time step (t) as demonstrated by Xie and Castro[28] to make filtering a 2D process in contrast to the 3D filtering originally proposed by Klein et al.[26] In equation 34, Δt is the time step and t_L is the Lagrangian time scale, such that $t_L = I_x/\bar{u}$.

$$\mathbf{v}_k^t = \mathbf{v}_k^{t-\Delta t} \exp\left(-\frac{\pi \Delta t}{2t_L}\right) + v_k^t \sqrt{1 - \exp\left(-\frac{\pi \Delta t}{t_L}\right)} \tag{34}$$

6. The final step involves the transformation originally proposed by Lund et al.[31] to obtain a time-dependent inflow velocity field. Components of a_{ij} are defined by the Reynolds-stress tensor, τ_{ij}, obtained from a previous RANS turbulent flat plate calculation performed on the same mesh as the LES simulation, at identical Mach and Reynolds numbers, using the $k-\epsilon$ turbulence model as described in Gerolymos.[32]

$$u_i = \overline{u}_i + a_{ij}\mathbf{v}_j^t \tag{35}$$

$$a_{ij} = \begin{bmatrix} \sqrt{\tau_{11}} & 0 & 0 \\ \tau_{21}/a_{11} & \sqrt{\tau_{22} - a_{21}^2} & 0 \\ \tau_{31}/a_{11} & (\tau_{32} - a_{21}a_{31})/a_{22} & \sqrt{\tau_{33} - a_{31}^2 - a_{32}^2} \end{bmatrix} \tag{36}$$

7. Lastly, the calculation of thermodynamic fluctuations was addressed by Touber and Sandham[30] by invoking the Strong Reynolds Analogy (SRA). However, they noted that the validity of such an assumption is debatable, since it holds true in a weak sense as shown by Guarini et al.[33] in a DNS simulation of Mach 2.5 supersonic turbulent boundary layer. Since the goal here is to provide an approximate first guess at the inflow plane, this approach was determined to be sufficient and is shown below:

$$\frac{T'}{\overline{T}} = -(\gamma - 1)M^2 \frac{u'}{\bar{u}} \qquad \text{where} \qquad M^2 = \frac{\bar{u}^2}{\gamma R \overline{T}} \tag{37}$$

8. Invoking SRA also means that the pressure fluctuations in the boundary layer are negligible, i.e., $p' = 0$. Thus, the following relation for the density fluctuations results:

$$\frac{\rho'}{\bar{\rho}} = -\frac{T'}{\overline{T}} \tag{38}$$

This concludes the procedure that produced the time-dependent fluctuating inflow plane. The filter parameters are provided in table 1. The separation unit spacing $(\Delta\alpha)$ in the y direction was obtained by picking an average spacing in the log-law region of the boundary layer, whereas grid spacing was picked in the z direction.

III. Simulation Methodology

A. Numerical Schemes

Spatial derivatives are calculated using a sixth-order compact spectral-like finite-difference scheme of Lele[34] and later adapted in the FDL3DI code by Visbal and Gaitonde.[35] An eighth-order low-pass Padé-type non-dispersive spatial filter is applied after each sub-iteration to maintain stability and dissipate energy

Table 1. Digital filter parameters

Parameter	x	y	z
Length Scale, I_α [a]	0.5	0.5	0.5
$\Delta\alpha$ [b]	-	0.01	0.0195
Equivalent Gridpoints, $M_\alpha = 2I_\alpha/\Delta\alpha$	-	50	25

[a] Non-dimensionalized by δ_{99}

[b] $\alpha = x, y, z$

in the high spatial wavenumber range where the turbulent energy spectrum is poorly resolved.[12,13] The filter coefficient, α_f, which determines sharpness of the filter cutoff was set to 0.45 based on Bisek[36] and Garmann et al.[37] The implicit time integration was performed with the second-order Beam-Warming[38] scheme using two Newton-like sub-iterations and approximate factorization. The non-dimensional time step for this problem was 0.002.

The use of an explicit sub-grid scale model is completely avoided in the present simulations since the intent is to study the budget of the exact equation of the Reynolds-stress transport. Such an approach was taken by Morgan et al.,[39] where flow conditions similar to the present study were used for $Re_\theta = 4800$ and comparisons were made with the DNS of Pirozzoli and Bernardini[40] which showed that at low to moderate Reynolds number, omitting an explicit sub-grid scale model is suitable. Kawai et al.[41] showed that inclusion of an explicit sub-grid scale model in addition to the low-pass filtering, as done in the present study, introduced excessive numerical dissipation of the resolved turbulence, which may underpredict turbulence statistics sought here. A comparison of high-fidelity implicit and sub-grid scale model LES for airfoils at low Reynolds number performed by Garmann et al.[37] showed no benefit in using an explicit sub-grid model. Thus, high-fidelity ILES, i.e., combination of high-order spatial scheme and high-order filter, is an attractive approach for this work as it is paired with well-resolved meshes in the near-wall region.

B. Boundary Conditions and Mesh Parameters

The flow conditions represent the experiments[5] performed at the Institut Universitaire des Systèmes Thermiques Industriel (IUSTI) in Marseille, France. Table 2 shows a comparison of experimental and simulated flow conditions. It is noted that to resolve the scales of turbulence corresponding to the experimental Reynolds number, a mesh several orders of magnitude larger than the fine mesh used here would be required. Thus, the simulated Reynolds number was varied, one matching that of the experiment and two others obtained by reducing the experimental Reynolds number by half successively. Reducing the Reynolds number allows the present work to be practical and achievable by ILES. Such an approach was also taken by Mullenix and Gaitonde,[42] Pirozzoli and Bernardini,[40] and Visbal et al.[43] In order to have consistent flow relations, the pressure was reduced by a factor of half and one-quarter while maintaining the temperature, when the Reynolds number was reduced. This assures that the Mach number and the velocity scales remain the same between the experiment and the simulation.

At the inflow of the computational domain, the digital filter was used to generate turbulent fluctuations and provide a turbulent boundary layer. The interior of the flowfield was initialized with the same RANS solution as the one used to impose the inflow boundary condition using the digital filter. The wall was treated as no-slip and adiabatic. The outflow and farfield boundaries were obtained by extrapolating values from the interior. A periodic boundary condition was applied in the z direction. The Rankine-Hugoniot relations were used to impose the oblique shock generated by a wedge in the experiment. Such a simulated shock was achieved by maintaining the farfield boundary condition for $x < x_{shock}$ at the pre-shock conditions identified in table 2, while $x > x_{shock}$ were set to the post-shock conditions obtained via oblique shock relations at Mach 2.29 and 8.0-degree angle of deflection.

In figure 2, the mesh schematic is presented where the coordinates are non-dimensionalized by the length scale δ_{99}. For the purpose of clarity, the coarse mesh is presented and every fourth point is shown. The mesh can be divided into two distinct sections in the streamwise direction: 1) the constant x-spacing section is where the SBLI occurs and 2) the coarsening to the outflow section. Both sections have the same hyperbolic tangent grid clustering in the y direction and a constant spacing in the z direction. Table 3 shows a list of

Table 2. Flow conditions upstream of the interaction region at $(x - x_{imp})/\delta_{99} = -5.7$

Property	Experiment	Simulation (nominal)
M_∞	2.29	2.29
U_∞, m/s	545.0	545.0
P_∞, Pa	50663	12600, 25300, 50663
T_0, K	300	300
δ_{99}, mm	10.0	11.0
θ, mm	0.87	0.87
δ^*, mm	3.0	3.1
Re_δ	53420	14500, 29000, 58000
Re_θ	4640	1150, 2300, 4600

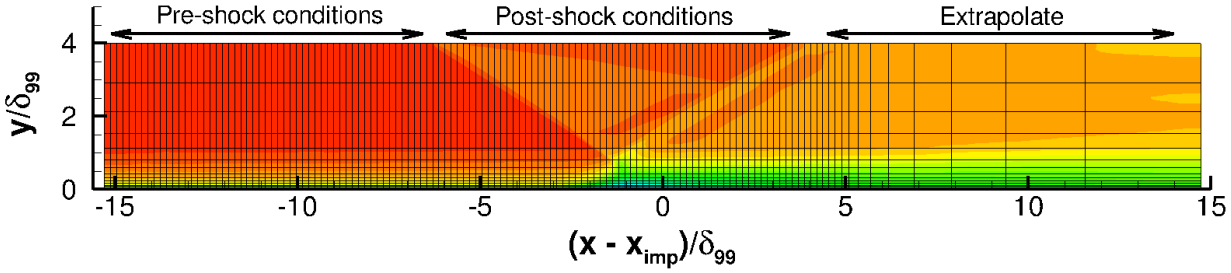

Figure 2. Mesh topology for SBLI simulation. Coordinates non-dimensionalized by the experimental δ_{99}. Every 8^{th} point in the x direction and 16^{th} point in the y direction is shown for clarity.

Table 3. Mesh parameters

	Coarse	Medium	Fine
Domain size			
$x \times y \times z$[a]	$30 \times 4 \times 5$	$30 \times 4 \times 5$	$30 \times 4 \times 5$
Computational points			
$N_x \times N_y \times N_z$	$1025 \times 257 \times 257$	$1537 \times 257 \times 257$	$2049 \times 257 \times 257$
N_{total}	67.7×10^6	101.5×10^6	135.35×10^6
Constant region			
N_x	945	1417	1889
Δx	0.0212	0.0141	0.0105
At $(x - x_{imp})/\delta_{99} = -5.7$			
Δx^+	15	10	7
$N_{y,bl}$	187	187	187
Δy_w	1×10^{-3}	1×10^{-3}	1×10^{-3}
Δy^+	0.68	0.68	0.68
Δz	0.0195	0.0195	0.0195
Δz^+	13	13	13

[a] x, y, z are non-dimensionalized by δ_{99}

parameters for coarse, medium, and fine meshes.

IV. Results

A. A Comparison with the Experiment

Normalized velocity, shown for various mesh levels in figure 3(a), is in agreement with the viscous sublayer. Coarse, medium, and fine meshes at $Re_\theta = 4600$ lined on top of each other and showed a slope that matched the expected logarithmic law (log law) of the wall ($\kappa = 0.41$ and $B = 5.5$), however an offset was present. Garnier et al.[44] also reported such a behavior where LES simulations were performed at $Re_\theta = 4600$ and the offset was attributed to the underprediction of the friction velocity, which showed small improvement with mesh refinement. Thus, this may indicate a lack of grid resolution in the log-law region. This is further supported by the coarse mesh solution at $Re_\theta = 2300$, which is in agreement with the log law, DNS of Pirozzoli and Bernardini,[40] and LES of Eitel-Amor[45] at $Re_\theta = 4400$. A comparison of skin friction profiles for the three mesh levels (figure 3(b)) show good agreement in the region upstream of the SBLI and within the SBLI, but some variation was present in the reattachment region. Thus, the current mesh resolution, although not as refined as the DNS presented in figure 3, is deemed suitable for the present simulation at experimental Reynolds number.

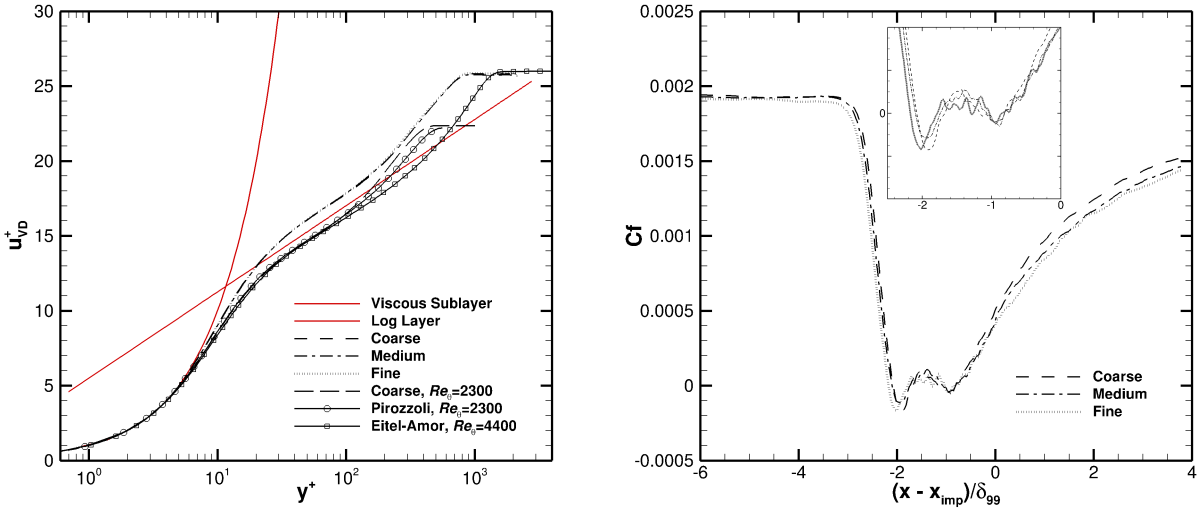

(a) van Driest transformed velocity profiles

(b) Skin friction

Figure 3. Upstream boundary layer at $(x - x_{imp})/\delta_{99} = -5.7$.

A comparison of interaction lengths, presented in table 4, show that the ILES and DNS simulations consistently underpredict the interaction region, including the present work. All simulations were done with periodic boundary conditions in the spanwise direction using an appropriate spanwise domain to avoid artificial amplification of the separation bubble. Thus, the rather good agreement obtained by Touber and Sandham[30] can be attributed to the choice of the subgrid-scale model[46] (Mixed-Time-scale). A separate RANS study was performed to better understand the interaction behavior relative to the choice of domain in the spanwise direction, i.e., periodic or half-span with one sidewall. Results, although omitted here for brevity, showed that the periodic simulations underpredicted the interaction length. The tunnel where the experiment was performed had an aspect ratio of 1.39 and the inverse viscous aspect ratio, δ_{99}/s, of 5.88×10^{-2}, thus characterized as quasi-two-dimensional,[6] but it is suggested by the authors of the present work that the experimental data was still influenced by sidewalls. Such a relation was hypothesized by Babinsky et al.[6] between the separation length and inverse viscous aspect ratio. At large and moderate inverse viscous aspect ratios, the corner separation and sidewall effects become critical in prediction of the interaction region at the tunnel centerline. Agostini et al.[47] noted that the interaction region can be underpredicted by up to 20%. In the LES simulation of Larchevêque et al.,[48] it was concluded that the interaction region produced by a 9.5° deflection case matched experiments with 8° and 8.8° deflections when performed by two different groups of researchers. Thus, only at sufficiently large span can such an experiment become two-dimensional and then a choice of periodic boundary condition would be accurate. So it can be

argued that the present ILES calculation simulates SBLI in such a large span wind tunnel and captures key physics void of corner separation and sidewalls. Hence making it more attractive for studying turbulence modeling.

Table 4. Comparison of previous and present simulations with the experimental data.

Authors	Nominal Re_θ	Interaction Length [a]	Simulation
Experiment[5]	4600	4.60	-
Touber and Sandham[30]	4600	4.80	Periodic/LES-SGS
Agostini et al.[47]	4600	3.45	Periodic/LES-SGS
Morgan et al.[39]	4800	2.90	Periodic/ILES
Morgan et al.[39]	2300	2.90	Periodic/ILES
Pirozzoli and Bernardini[40]	2300	2.89	Periodic/DNS
Present work	4600	2.94	Periodic/ILES
Present work	2300	3.06	Periodic/ILES

[a] Non-dimensionalized by δ_{99}, i.e., L_{int}/δ_{99}

A qualitative comparison with the experiment is presented in figure 4, where the coordinates have been scaled by the respective interaction lengths. Key features like the undisturbed boundary-layer, turning of the flow over the separation bubble, and the boundary-layer recovery can be observed in figures 4(a) and 4(b). Locations of high stress also coincide, however the magnitudes differ due to the aforementioned underprediction of the interaction length. Undisturbed boundary-layer stress profiles, figure 5, show that the streamwise stress is in good agreement with the data and the near-wall peak is captured, but disagreement exists in the outer part of the boundary layer. The discrepancy begins at $y/\delta_{99} = 0.3$, which happens to be the boundary-layer displacement thickness. An opposite trend was observed with the wall-normal stress, i.e., better agreement was obtained in the outer part of the boundary layer. Touber and Sandham[49] reported similar behavior in their work, even though they used a zonal digital filter approach in the wall-normal direction. A separate study, results not included here, examined the impact of digital filter length scales (cf. table 1) and possible improvements in generation of fluctuations at the inflow plane. Among items under further consideration are zonal implementation to impose the relevant length scales in the wall-normal direction and *in situ* calculation of relevant length scales in the streamwise direction.

B. Reynolds-stress Budgets

1. *Validation of Budgets*

The budget of the Reynolds-stress transport and the imbalance in the budget was calculated at the undisturbed upstream location $(x - x_{imp})/\delta_{99} = -5.7$ for $Re_\theta = 2300$ and 4600. The imbalance highlights the relative magnitude of each term and should be zero if production, transfer, and dissipation mechanisms that govern the energy cascade are appropriately captured. A non-zero value is an indication of the error in the solution. To calculate the imbalance, unsteady term was assumed to be negligible in equation 2 and the convective term was subtracted from the right-hand side to yield equation 39.

$$\text{Imbalance} = \mathcal{P}_{ij} + \mathcal{D}_{ij} - \bar{\rho}\epsilon_{ij} + \Pi_{ij} + \mathcal{M}_{ij} - \frac{\partial}{\partial x_k}(\overline{\rho u_i'' u_j''}\tilde{u}_k) = 0 \tag{39}$$

The turbulent kinetic energy (TKE) budget was calculated by taking one-half of the trace of the Reynolds-stress budget. The present TKE budget is similar to the Mach 2.5 DNS of Guarini et al.[33] and the Mach 4 DNS of Sinha et al.[50] Both examined a turbulent boundary layer and are thus relevant to the current work. A comparison of TKE budget with the finely-resolved incompressible LES of Eitel-Amor[45] (figure 6) at $Re_\theta = 4400$ shows good agreement, especially in the viscous sublayer and log-law regions. Differences in the peak of production and troughs of molecular and turbulent diffusion within the buffer region ($10 \leq y^+ \leq 30$) can be attributed to the vast difference in mesh resolution. The terms related to compressibility, i.e., pressure strain and turbulent mass flux were small and thus omitted from figure 6. The imbalance reached a peak in the buffer region with a value of 0.056, approximately four times larger than the LES of Eitel-Amor.[45]

$$k = \frac{1}{2} tr(\overline{\rho u_i'' u_j''}) \tag{40}$$

Budgets are plotted for the normal stresses and the primary shear stress in figure 7. To lend confidence to the present calculations, the results are plotted alongside a turbulent boundary layer spectral DNS of Schlatter and Örlü.[51] The present results also look similar to the turbulent channel flow DNS of Mansour et al.,[19] Spalart's[18] DNS of a turbulent boundary layer, and turbulent square duct DNS of Huser et al.[20] It is noted however that these works examining the budget relied on the incompressible form of equation 2. Moreover, the pressure-velocity correlation was expressed by combining the pressure diffusion (equation 7) and pressure strain (equation 8) terms as shown in equation 41, so some discrepancy in figure 7 is due to the fact that the available Schlatter and Örlü[51] data is of the total velocity-pressure correlation.

$$\Pi_{ij}^{tot} = \mathcal{D}_{ij}^{P} + \Pi_{ij} = -\overline{u_i'' \frac{\partial p'}{\partial x_j}} - \overline{u_j'' \frac{\partial p'}{\partial x_i}} \tag{41}$$

Since the following comparison is presented in the undisturbed part of the upstream boundary layer at $(x - x_{imp})/\delta_{99} = -5.7$, $\overline{\rho u'' w''}$ and $\overline{\rho v'' w''}$ were negligible as expected. The $\overline{\rho u'' u''}$ budget shows molecular diffusion in balance with dissipation at the wall, however, away from the wall and in the buffer region, peak production is balanced by dissipation, pressure strain, and diffusion terms. In the log-law region, molecular and turbulent diffusion become less dominant, thus production is balanced by dissipation and pressure strain terms. In the $\overline{\rho v'' v''}$ and $\overline{\rho w'' w''}$ budgets, figures 7(b) and 7(c), the pressure strain term assumed a dominant role and governed the transfer of energy to these normal stresses. Huser et al.[20] concluded that near the wall pressure strain and pressure diffusion are of opposite value and thus cancel, so the pressure-velocity should be modeled using equation 41, however that is only true for off-diagonal components of these two terms. While off-diagonal terms do not vanish at the wall, the diagonal pressure strain naturally goes to zero and pressure diffusion is negligible at the wall as shown by the present calculation. Knowing this behavior Mansour et al.[19] suggested that a possible model for pressure-velocity correlation should be based on the trace of equation 41. However, the role of the pressure strain term as an energy transfer mechanism is the reason that the term (equation 8) is directly modeled in recent contemporary Reynolds-stress turbulence models.[52]

For both $\overline{\rho v'' v''}$ and $\overline{\rho w'' w''}$, the pressure strain term is balanced by dissipation in the region away from the wall. In the case of $\overline{\rho v'' v''}$ the peak in the pressure strain occured at the beginning of the log-law region, indicating wall-normal ejection of energy packets, while the peak in $\overline{\rho w'' w''}$ occurs at the end of the viscous sublayer. Finally, the budget of $\overline{\rho u'' v''}$, examined in figure 7(d), shows that in the viscous sublayer region a positive dissipation is balanced by a negative molecular diffusion and away from the wall a negative production is balanced by positive turbulent diffusion, pressure diffusion, and pressure strain. This may seem counterintutive but because shear stress can either be positive or negative, a negative value of larger magnitude means higher shear stress and vice versa.

The effect of the Reynolds number scaling is investigated by comparing $\overline{\rho u'' u''}$ at three simulated Reynolds numbers (figure 8) for the coarse mesh. The lowest peak imbalance in the sum of the budget for the smallest Reynolds number was indicative of the fact that the coarse mesh was sufficiently resolved. But for the higher Reynolds numbers, small increases in the peak imbalance were observed, which corresponded to the smaller dissipation term. Thus, suggesting that the simulations at higher Reynolds numbers were approaching the limit where ILES would still be valid and may potentially benefit from an increase in the mesh resolution. The largest Reynolds number had a peak in the budget imbalance of 0.09 for the coarse mesh. The peak in the imbalance dropped to 0.08 for the fine mesh, implying that the meshes used in the present work are sufficient for ILES and significantly large numbers of grid points would be necessary to drive the imbalance to zero. This was further supported by the similarity in wall properties between the present fine mesh and Poggie's[53] Grid 2 and Grid 3. Poggie[53] performed a detailed mesh resolution study for a turbulent boundary layer at similar flow conditions, where Re_θ ranged from approximately $1300 - 2000$ and mesh sizes ranged from 1.1×10^7 to 3.3×10^{10}. Although budgets were not computed in his work, the Reynolds stress profiles showed no change beyond Grid 3. Thus, from this point onward, the fine mesh results will be presented for the budgets.

2. *Budgets in Shock wave/Boundary-layer Interaction*

The budgets of Reynolds stress within the SBLI region are presented next. Figures 9 to 11 show comparisons at the pre-reflected-shock, post-reflected-shock, separation bubble, and post-impinging-shock locations. Since the friction velocity becomes small in the SBLI region, normalizing the budgets by $\rho_w u_\tau^4/\nu_w$ becomes ineffective. In the absence of a new means of normalization, this section omitted the aforementioned normalization in favor of the non-dimensionalization employed in equations (17a) and (17b), i.e., freestream conditions $\rho_\infty U_\infty^4/\nu_\infty$. The ordinate axis still utilizes the inner scaling since the friction velocity only has a first-order effect on y^+.

Budgets in figure 7 are replotted in figure 9 with the freestream normalization (left panel) and compared with the post-reflected-shock budgets (right panel). The $\overline{\rho u'' u''}$ component in figures 9(a) and 9(b) showed a threefold increase in the peak production, which was balanced by the turbulent diffusion and an amplification in the pressure strain term. The increased dissipation at the wall was balanced by the molecular diffusion and pressure strain terms. Previously inactive terms like turbulent mass flux and convection also showed a significant increase. This resulted in a net gain in the budget imbalance for the component, however this was expected. The unsteady term in equation 2 was assumed to be zero in order to calculate the imbalance, while such an approach was valid for the undisturbed boundary layer, the assumption wouldn't be accurate in the presence of characteristically low-frequency oscillations of the reflected shock/separation region. The abrupt increase in the production leads to a lag in the energy transfer mechanisms, followed by the increased anisotropy and the budget imbalance. In other words, the budget imbalance could be thought of as the unsteady contribution, which becomes significant in the interaction region.

The secondary normal stresses, $\overline{\rho v'' v''}$ and $\overline{\rho w'' w''}$, are shown in figures 9(c) to 9(f). Notice that the post-reflected-shock budgets have ordinate axes an order of magnitude larger than the pre-reflected-shock budgets. The proportional behavior of pressure diffusion and pressure strain terms remained the same for $\overline{\rho v'' v''}$ in the near wall region, while away from the wall, convection, turbulent diffusion, and production terms came to prominence. For $\overline{\rho w'' w''}$, the near-wall dissipation was balanced by molecular diffusion and pressure strain terms, a relationship that remained proportional. Here, however, only the convection term became important away from the wall. It is important to point out that the role pressure strain and pressure diffusion terms play, as agents of energy transfer, remained unchanged and became amplified in the presence of the shock. The artifact present at $y^+ \sim 250$ was due to the profiles crossing the reflected shock, thus significant for $\overline{\rho v'' v''}$ and absent for $\overline{\rho w'' w''}$ due to the 2D nature of the shock.

Figure 10 shows budgets in the separation bubble (left panel) and the post-impinging-shock recovery region (right panel). Examining $\overline{\rho u'' u''}$ in figures 10(a) and 10(b), it was clear that in the near-wall region molecular diffusion and pressure strain terms balanced dissipation, which established the key role pressure strain played in the interaction region and it's residual importance in the post-impinging-shock recovery region. The peak production at $y^+ \sim 50$ corresponds to the high stress region (figure 4(c)) above the separation bubble. This high rate of production was balanced by pressure strain, turbulent transport, and convection terms. Further away from the wall at $y^+ \sim 100$, another area of activity corresponds to the impinging shock, where pressure diffusion and pressure strain terms become prominent and balanced by production and turbulent mass flux terms. Lastly, the fluctuation at $y^+ \sim 250$ was due to the reflected shock. Similarly in the recovery region a two-peak behavior was observed for the production term. The first peak at $y^+ \sim 10$ was representative of a typical turbulent boundary layer, but lower in magnitude since the boundary layer was not fully recovered. While the second peak at $y^+ \sim 300$ was due to the high stress region that continued past the interaction region. The secondary normal stresses showed a similar behavior as $(x - x_{imp})/\delta_{99} = -2.0$, however the terms in the recovery region had lower magnitudes as expected.

Finally, the primary shear stress, $\overline{\rho u'' v''}$, is presented in figure 11 for all four locations. Notice that the ordinate axis is an order of magnitude higher for budgets in the interaction region. It was also clipped to highlight terms with smaller magnitudes, however the near-wall peak values of pressure strain and pressure diffusion terms are stated on the plots. Both terms maintain proportionality at the wall and cancel each other, but a large increase in the magnitude was observed. Away from the wall and in the undisturbed boundary layer, pressure strain and pressure diffusion terms jointly balanced the negative production term, whereas in the interaction and recovery regions a new layer of high pressure strain and pressure diffusion developed, albeit with reversed signs compared to the wall. This behavior was most prominent in the post-reflected-shock region and diminished at aft locations. Previously benign terms like turbulent transport and turbulent mass flux also played a role to balance the negative production term, especially in the region confined between the separation bubble and the crossing of the impinging and reflected shocks.

V. Conclusions

Implicit large-eddy simulations (ILES) of a *two-dimensional* shock wave/boundary-layer interaction (SBLI) were performed. Comparisons with the experiment showed that the interaction region was underpredicted. This was attributed to the role sidewalls and corner influences played on the tunnel centerline, despite the fact that the experiment was claimed to be void of three-dimensional effects. This conclusion was supported by contemporary studies of other authors and could be validated by performing a three-dimensional, full-span, two-sidewall simulation, currently under consideration. Thus, the present simulation, which employed periodic boundary conditions in the spanwise direction was truly two-dimensional and valuable for turbulence model development and validation.

Budgets were computed for the Reynolds-stress transport equation and validated against previous highly-resolved LES and DNS simulations of a turbulent boundary layer, channel flow, and a square duct. Grid resolution in the y and z directions was deemed sufficient for ILES, thus grid resolution in only the x direction was studied. It was shown that the coarse mesh was adequate for the current flow conditions. However, an investigation to assess the ability of the coarse mesh to resolve the scale of turbulence by reducing the Reynolds number of the simulation by half and one-quarter showed that the budget imbalance dropped as the Reynolds number was reduced. This indicated that the imbalance in the budget shown for the undisturbed boundary layer, at the largest Reynolds number, was due to the mesh not supporting the smallest of the scales to dissipate the energy. Interestingly, this also meant that the approach of using a high-order low-pass filter in lieu of a subgrid-scale model was valid as it added minimal numerical dissipation, but this was not quantified here.

Budgets within the SBLI showed an advantage in studying the pressure strain and pressure diffusion terms separately. They cancelled each other at the wall but their behavior was different away from the wall. While the pressure diffusion term remained small but non-zero for the normal stress budgets, it assumed an important role in the primary shear stress budgets and in one instance it was the same order of magnitude as the pressure strain term near the wall. Thus, Reynolds stress turbulence models could show improvement by accounting for the pressure diffusion term rather than the current practice of some model developers to assume it negligible or include it into the model for turbulent diffusion. Moreover, the pressure strain term continued to play a key role in the transfer of energy from the primary normal stress to the secondary normal stresses, which makes it an important term to model, as is the case with Reynolds stress turbulence models in use today.

Acknowledgments

The authors would like to thank NASA's Transformative Aeronautics Concepts Program and Transformational Tools and Technology Project for its generous support. Resources supporting this work were provided by the NASA High-End Computing (HEC) Program through the NASA Advanced Supercomputing (NAS) Division at Ames Research Center.

References

[1]Dolling, D. S., "Fifty Years of Shock-Wave/Boundary-Layer Interaction Research: What Next?" *AIAA Journal*, Vol. 39, No. 8, August 2001, pp. 1517–1531.

[2]Zheltovodov, A. A., "Some Advances in Research of Shock Wave/Turbulent Boundary-layer Interactions," No. 0496 in 44th Aerospace Sciences Meeting, American Institute of Aeronautics and Astronautics, January 2006.

[3]Gaitonde, D. V., "Progress in Shock Wave/Boundary Layer Interactions," No. 2607 in 43rd Fluid Dynamics Conference, American Institute of Aeronautics and Astronautics, June 2013.

[4]Souverein, L. J., Dupont, P., Debiève, J.-F., Dussauge, J.-P., van Oudheusden, B. W., and Scarano, F., "Effect of Interaction Strength on Unsteadiness in Turbulent Shock Wave Induced Separations," *AIAA Journal*, Vol. 48, No. 7, July 2010, pp. 1480–1493.

[5]Dussauge, J.-P., Dupont, P., and Debiève, J.-F., "Unsteadiness in Shock Wave Boundary Layer Interactions with Separations," *Aerospace Science and Technology*, Vol. 10, No. 2, December 2006, pp. 85–91.

[6]Babinsky, H., Oorebeek, J., and Cottingham, T. G., "Corner Effects in Reflecting Oblique Shock-wave/Boundary-layer Interactions," No. 0859 in 51st Aerospace Sciences Meeting, American Institute of Aeronautics and Astronautics, January 2013.

[7]Benek, J. A., Casimir J. Suchyta, I., and Babinsky, H., "The Effect of Wind Tunnel Size on Incipient Shock Boundary Layer Interaction Experiments," No. 0862 in 51st Aerospace Sciences Meeting, American Institute of Aeronautics and Astronautics, January 2013.

[8]Benek, J. A., Casimir J. Suchyta, I., and Babinsky, H., "The Effect of Wind Tunnel Size and Shock Strength on

Incident Shock Boundary Layer Interaction Experiments," No. 3336 in 44th Fluid Dynamics Conference, American Institute of Aeronautics and Astronautics, June 2014.

[9]Eagle, W. E., Driscoll, J. F., and Benek, J. A., "Experimental Investigation of Corner Flows in Rectangular Supersonic Inlets with 3D Shock-Boundary Layer Effects," No. 0857 in 49th Aerospace Sciences Meeting, American Institute of Aeronautics and Astronautics, January 2011.

[10]Clemens, N. T. and Narayanaswamy, V., "Low-frequency Unsteadiness of Shock Wave/Turbulent Boundary Layer Interactions," *The Annual Review of Fluid Mechanics*, Vol. 46, January 2014, pp. 469–492.

[11]Georgiadis, N. J., Rizzetta, D. P., and Fureby, C., "Large-eddy Simulations: Current Capabilities, Recommended Practices, and Future Research," *AIAA Journal*, Vol. 48, No. 8, August 2010, pp. 1772–1784.

[12]Gaitonde, D. V. and Visbal, M. R., "Padé-type Higher-order Boundary Filters for the Navier-Stokes Equations," *AIAA Journal*, Vol. 38, No. 11, November 2000, pp. 2103–2112.

[13]Visbal, M. R., Morgan, P. E., and Rizzetta, D. P., "An Implicit LES Approach Based on High-order Compact Differencing and Filterning Schemes," No. 4098 in 16th Computational Fluid Dynamics Conference, American Institute of Aeronautics and Astronautics, June 2003.

[14]DeBonis, J. R., Oberkampf, W. L., Wolf, R. T., Orkwis, P. D., Turner, M. G., Babinsky, H., and Benek, J. A., "Assessment of Computational Fluid Dyanmics and Experimental Data for Shock Boundary-layer Interactions," *AIAA Journal*, Vol. 50, No. 4, April 2012, pp. 891–903.

[15]Hamlington, P. E. and Dahm, W. J. A., "Reynolds Stress Closure for Nonequilibrium Effects in Turbulent Flows," *Physics of Fluids*, Vol. 20, No. 11, November 2008.

[16]Sinha, K., Mahesh, K., and Candler, G. V., "Modeling Shock Unsteadiness in Shock/Turbulence Interaction," *Physics of Fluids*, Vol. 15, No. 8, August 2003, pp. 2290–2297.

[17]Vyas, M. A., Waindim, M., and Gaitonde, D. V., "Budget of Turbulent Kinetic Energy in a Shock Wave/Boundary-layer Interaction," No. 3187 in 46th Fluid Dynamics Conference, American Institute of Aeronautics and Astronautics, June 2016.

[18]Spalart, P. R., "Direct Simulation of a Turbulent Boundary Layer up to $R_\theta = 1410$," *Journal of Fluid Mechanics*, Vol. 187, May 1988, pp. 61–98.

[19]Mansour, N. N., Kim, J., and Moin, P., "Reynolds Stress and Dissipation Rate Budgets in a Turbulent Channel Flow," *Journal of Fluid Mechanics*, Vol. 194, June 1988, pp. 15–44.

[20]Huser, A., Biringen, S., and Hatay, F. F., "Direct Numerical Simulation of Turbulent Flow in a Square Duct: Reynolds Stress Budgets," No. 0187 in 32nd Aerospace Sciences Meeting, American Institute of Aeronautics and Astronautics, January 1994.

[21]Gaitonde, D. V. and Visbal, M. R., "High-order Schemes for Navier-Stokes Equations: Algorithm and Implementation into FDL3DI," Technical Report 3060, Air Force Research Laboratory, August 1998.

[22]Anderson, D. A., Tannehill, J. C., and Pletcher, R. H., *Computational Fluid Mechanics and Heat Transfer*, Computational Methods in Mechanics and Thermal Sciences, Hemisphere Publishing Corporation, 1984.

[23]Shyy, W., Jayaraman, B., and Andersson, A., "Modeling of Glow Discharge-induced Fluid Dynamics," *Journal of Applied Physics*, Vol. 92, No. 11, December 2002, pp. 6434–6443.

[24]Gaitonde, D. V., Visbal, M. R., and Roy, S., "Control of Flow Past a Wing Section with Plasma-based Body Forces," No. 5302 in 36th Plasmadynamics and Lasers Conference, American Institute of Aeronautics and Astronautics, June 2005.

[25]Mullenix, N. J., Gaitonde, D. V., and Visbal, M. R., "Spatially Developing Supersonic Turbulent Boundary Layer with a Body-Force-Based Method," *AIAA Journal*, Vol. 51, No. 8, August 2013, pp. 1805–1819.

[26]Klein, M., Sadiki, A., and Janicka, J., "A Digital Filter Based Generation of Inflow Data for Spatially Developing Direct Numerical or Large Eddy Simulations," *Journal of Computational Physics*, Vol. 186, February 2003, pp. 652–665.

[27]Veloudis, I., Yang, Z., McGuirk, J. J., Page, G. J., and Spencer, A., "Novel Implementation and Assessment of a Digital Filter Based Approach for the Generation of LES Inlet Conditions," *Flow, Turbulence and Combustion*, Vol. 79, March 2007, pp. 1–24.

[28]Xie, Z.-T. and Castro, I. P., "Efficient Generation of Inflow Conditions for Large Eddy Simulation of Street-scale Flows," *Flow, Turbulence and Combustion*, Vol. 81, April 2008, pp. 449–470.

[29]Pope, S. B., *Turbulent Flows*, Cambridge University Press, 8th ed., 2011.

[30]Touber, E. and Sandham, N. D., "Oblique Shock Impinging on a Turbulent Boundary Layer: Low-Frequency Mechanisms," No. 4170 in 38th Fluid Dynamics Conference, American Institute of Aeronautics and Astronautics, June 2008.

[31]Lund, T. S., Wu, X., and Squires, K. D., "Generation of Turbulent Inflow Data for Spatially-developing Boundary-layer Simulations," *Journal of Computational Physics*, Vol. 140, 1998, pp. 233–258.

[32]Gerolymos, G. A., "Implicit Multiple-grid Solution of the Compressible Navier-Stokes Equations Using $k - \epsilon$ Turbulence Closure," *AIAA Journal*, Vol. 28, No. 10, October 1990, pp. 1707–1717.

[33]Guarini, S. E., Moser, R. D., Shariff, K., and Wray, A., "Direct Numerical Simulation of a Supersonic Turbulent Boundary Layer at Mach 2.5," *Journal of Fluid Mechanics*, Vol. 414, January 2000, pp. 1–33.

[34]Lele, S. K., "Compact Finite Difference Scheme with Spectral-like Resolution," *Journal of Computational Physics*, Vol. 103, August 1992, pp. 16–42.

[35]Visbal, M. R. and Gaitonde, D. V., "On the Use of High-order Finite-difference Schemes on Curvilinear and Deforming Meshes," *Journal of Computational Physics*, Vol. 181, May 2002, pp. 155–185.

[36]Bisek, N. J., "High-order Implicit Large-eddy Simulations of a Supersonic Corner Flow over a Compression Ramp," No. 3335 in 44th Fluid Dynamics Conference, American Institute of Aeronautics and Astronautics, June 2014.

[37]Garmann, D. J., Visbal, M. R., and Orkwis, P. D., "Comparative Study of Implicit and Subgrid-scale Model Large-eddy Simulation Techniques for Low-Reynolds Number Airfoil Applications," *International Journal for Numerical Methods in Fluids*, Vol. 71, August 2013, pp. 1546–1565.

[38]Beam, R. M. and Warming, R. F., "An Implicit Factored Scheme for the Compressible Navier-Stokes Equations," *AIAA Journal*, Vol. 16, No. 4, April 1978, pp. 393–402.

[39]Morgan, B., Duraisamy, K., Nguyen, N., Kawai, S., and Lele, S. K., "Flow Physics and RANS Modelling of Oblique Shock/Turbulent Boundary Layer Interaction," *Journal of Fluid Mechanics*, Vol. 729, July 2013, pp. 231–284.

[40]Pirozzoli, S. and Bernardini, M., "Direct Numerical Simulation Database for Impinging Shock Wave/Turbulent Boundary-layer Interaction," *AIAA Journal*, Vol. 49, No. 6, June 2011, pp. 1307–1312.

[41]Kawai, S., Shankar, S. K., and Lele, S. K., "Assessment of Localized Artificial Diffusivity Scheme for Large-eddy Simulation of Compressible Turbulent Flows," *Journal of Computational Physics*, Vol. 229, November 2010, pp. 1739–1762.

[42]Mullenix, N. J. and Gaitonde, D. V., "Analysis of Unsteady Behavior in Shock/Turbulent Boundary Layer Interactions with Large-Eddy Simulations," No. 0404 in 51st Aerospace Sciences Meeting, American Institute of Aeronautics and Astronautics, January 2013.

[43]Visbal, M. R., Rizzetta, D. P., and Mathew, J., "Large-eddy Simulations of Flow Past a 3-D Bump," No. 0917 in 45th Aerospace Sciences Meeting, American Institute of Aeronautics and Astronautics, January 2007.

[44]Garnier, E., Sagaut, P., and Deville, M., "Large Eddy Simulation of Shock/Boundary-layer Interaction," *AIAA Journal*, Vol. 40, No. 10, October 2002, pp. 1935–1944.

[45]Eitel-Amor, G., Örlü, R., and Schlatter, P., "Simulation and Validation of a Spatially Evolving Turbulent Boundary Layer up to $Re_\theta = 8300$," *International Journal of Heat and Fluid Flow*, Vol. 47, 2014, pp. 57–69.

[46]Inagaki, M., Kondoh, T., and Nagano, Y., "A Mixed-Time-Scale SGS Model With Fixed Model Parameters for Practical LES," *Journal of Fluids Engineering*, Vol. 127, January 2005, pp. 1–13.

[47]Agostini, L., Larchevêque, L., Dupont, P., Debiève, J.-F., and Dussauge, J.-P., "Zones of Influence and Shock Motion in a Shock/Boundary-layer Interaction," *AIAA Journal*, Vol. 50, No. 6, June 2012, pp. 1377–1387.

[48]Larchevêque, L., Dupont, P., de Martel, E., Garnier, E., and Debieve, J.-F., "Experimental and Numerical Study of Unsteadiness in Boundary Layer/ Shock Wave Interaction," *Turbulence and Interactions*, , No. 110, 2010, pp. 263–269.

[49]Touber, E. and Sandham, N. D., "Large-eddy Simulations of Low-frequency Unsteadiness in a Turbulent Shock-induced Separation Bubble," *Theoretical and Computational Fluid Dynamics*, Vol. 23, May 2009, pp. 79–107.

[50]Sinha, K., Martín, M. P., and Candler, G. V., "Assessment of the $k - \epsilon$ Turbulence Model for Compressible Flows using Direct Simulation Data," No. 0730 in 39th Aerospace Sciences Meeting, American Institute of Aeronautics and Astronautics, January 2001.

[51]Schlatter, P. and Örlü, R., "Assessment of Direct Numerical Simulation Data of Turbulent Boundary Layers," *Journal of Fluid Mechanics*, Vol. 659, July 2010, pp. 116–126.

[52]Cécora, R.-D., Radespiel, R., Eisfeld, B., and Probst, A., "Differential Reynolds-stress Modeling for Aeronautics," *AIAA Journal*, Vol. 53, No. 3, March 2015, pp. 739–755.

[53]Poggie, J., Bisek, N. J., and Gosse, R., "Resolution Effects in Compressible, Turbulent Boundary Layer Simulations," *Computer and Fluids*, Vol. 120, July 2015, pp. 57–69.

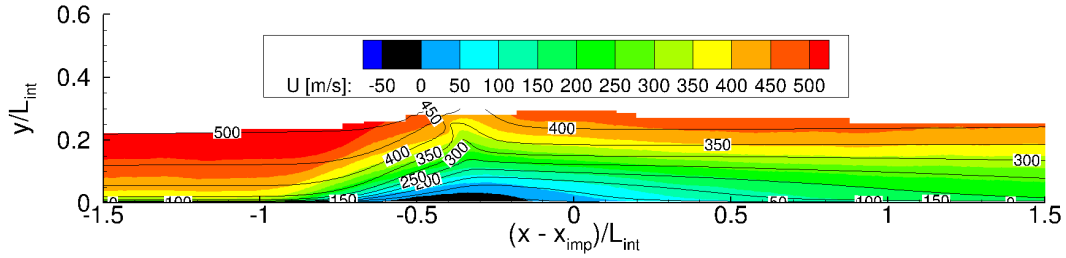

(a) $\overline{u}$

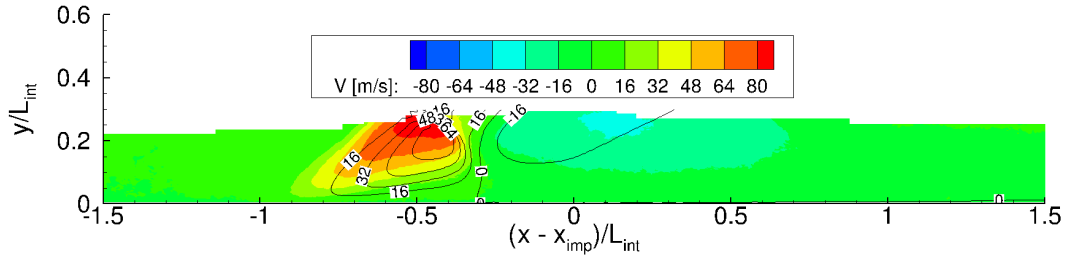

(b) $\overline{v}$

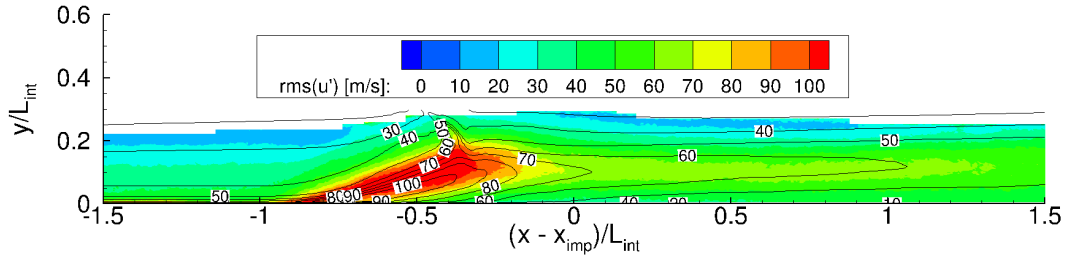

(c) $\sqrt{\overline{u'u'}}$

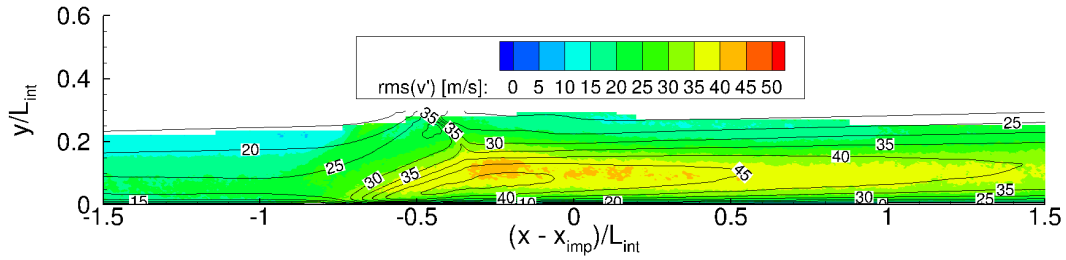

(d) $\sqrt{\overline{v'v'}}$

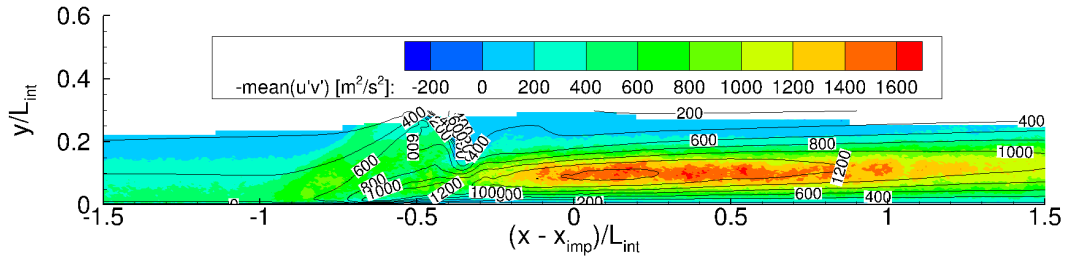

(e) $-\overline{u'v'}$

Figure 4. Mean velocity, normal stress, and shear stress comparisons at $Re_\theta = 4600$. Simulation is shown with labeled lines and overlaid on experimental data contours. Both share the same legend.

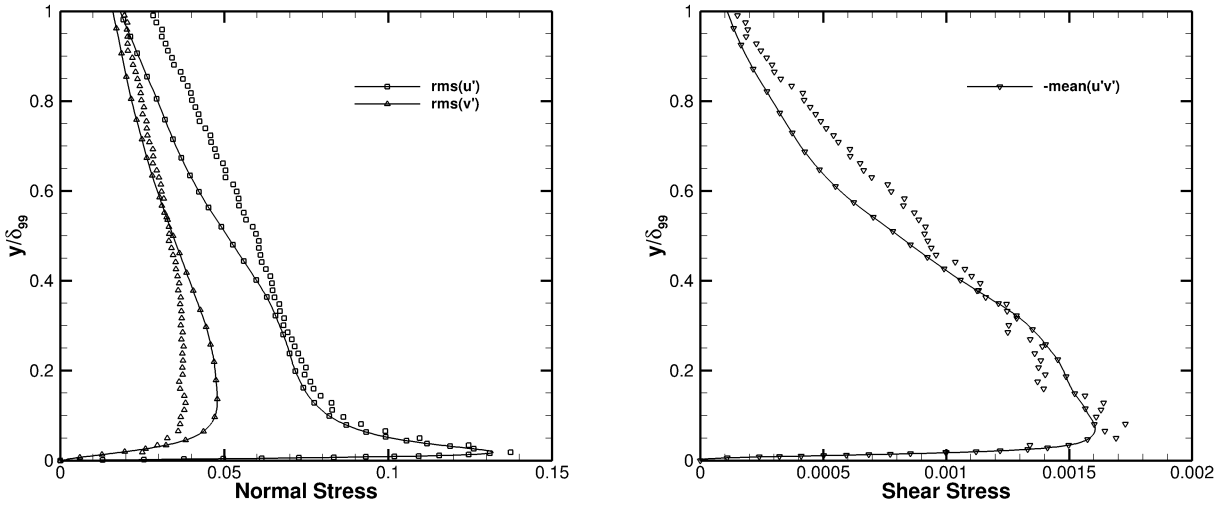

(a) $\sqrt{\overline{u'^2}}$ and $\sqrt{\overline{v'^2}}$ (b) $-\overline{u'v'}$

Figure 5. Stress profiles comparison at $(x - x_{imp})/\delta_{99} = -5.7$ for $Re_\theta = 4600$. Markers without lines represent experimental data.

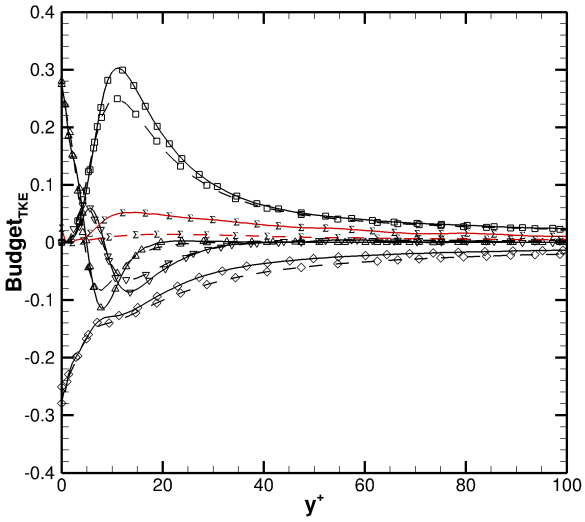

Figure 6. Budget of the turbulent kinetic energy at $(x - x_{imp})/\delta_{99} = -5.7$. Present results (solid lines) at $Re_\theta = 4600$ compared with LES of Eitel-Amor[45] (dashed lines) at $Re_\theta = 4400$. □: Production, △: Molecular diffusion, ▽: Turbulent diffusion, ◇: dissipation, and Σ: Sum. Budgets have been normalized by $\rho_w u_\tau^4/\nu_w$.

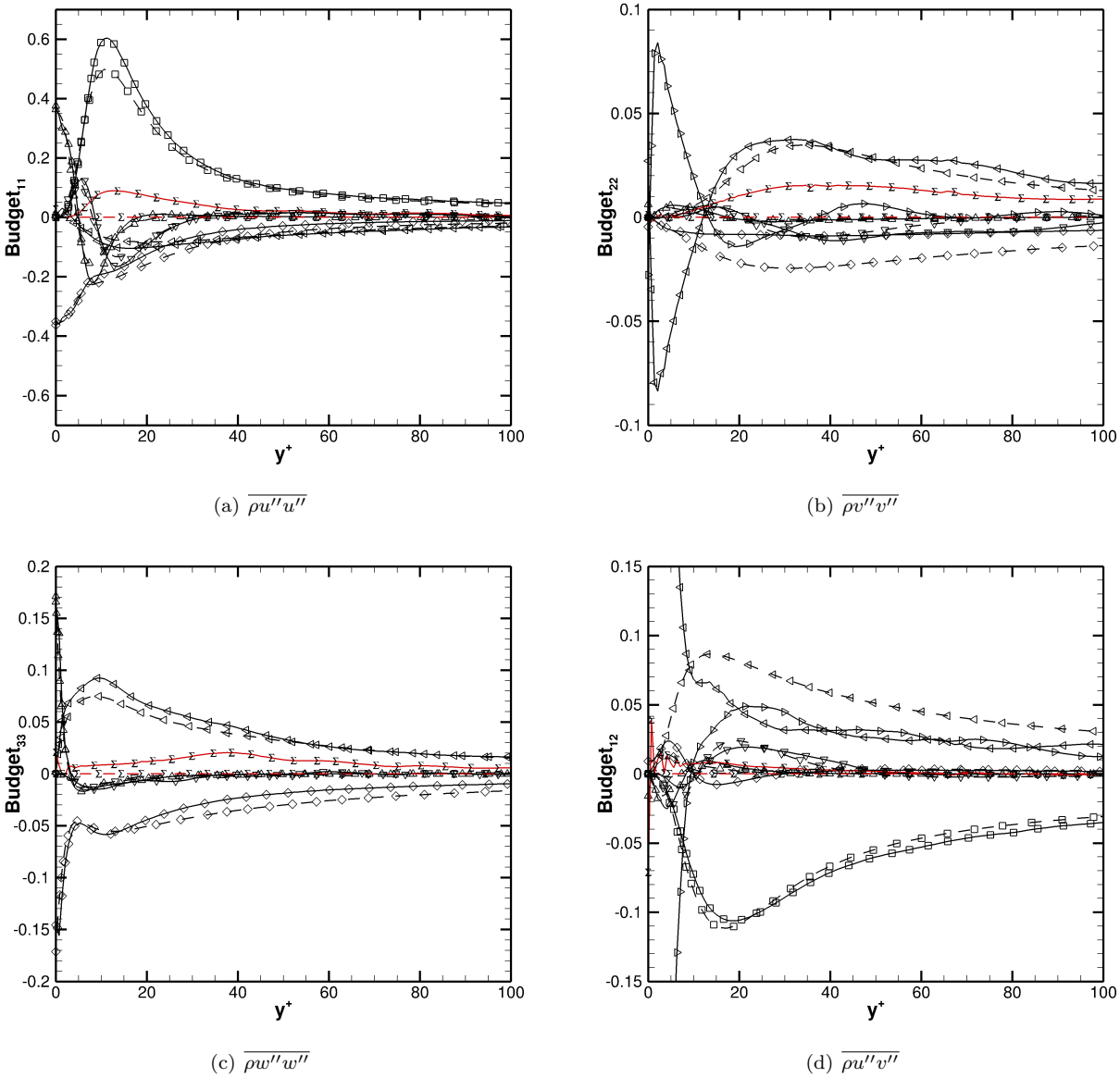

(a) $\overline{\rho u'' u''}$ (b) $\overline{\rho v'' v''}$

(c) $\overline{\rho w'' w''}$ (d) $\overline{\rho u'' v''}$

Figure 7. Reynolds-stress budget at $(x - x_{imp})/\delta_{99} = -5.7$. Present results (solid lines) at $Re_\theta = 4600$ compared with DNS of Schlatter and Örlü[51] (dashed lines) at $Re_\theta = 4000$. □: Production, △: Molecular diffusion, ▽: Turbulent diffusion, ▷: Pressure diffusion, ◁: Pressure strain, ♢: dissipation, ◯: Turbulent mass flux, X: Convection, and Σ: Sum. Terms smaller than three orders of magnitude are omitted from the plots for clarity. Budgets have been normalized by $\rho_w u_\tau^4/\nu_w$.

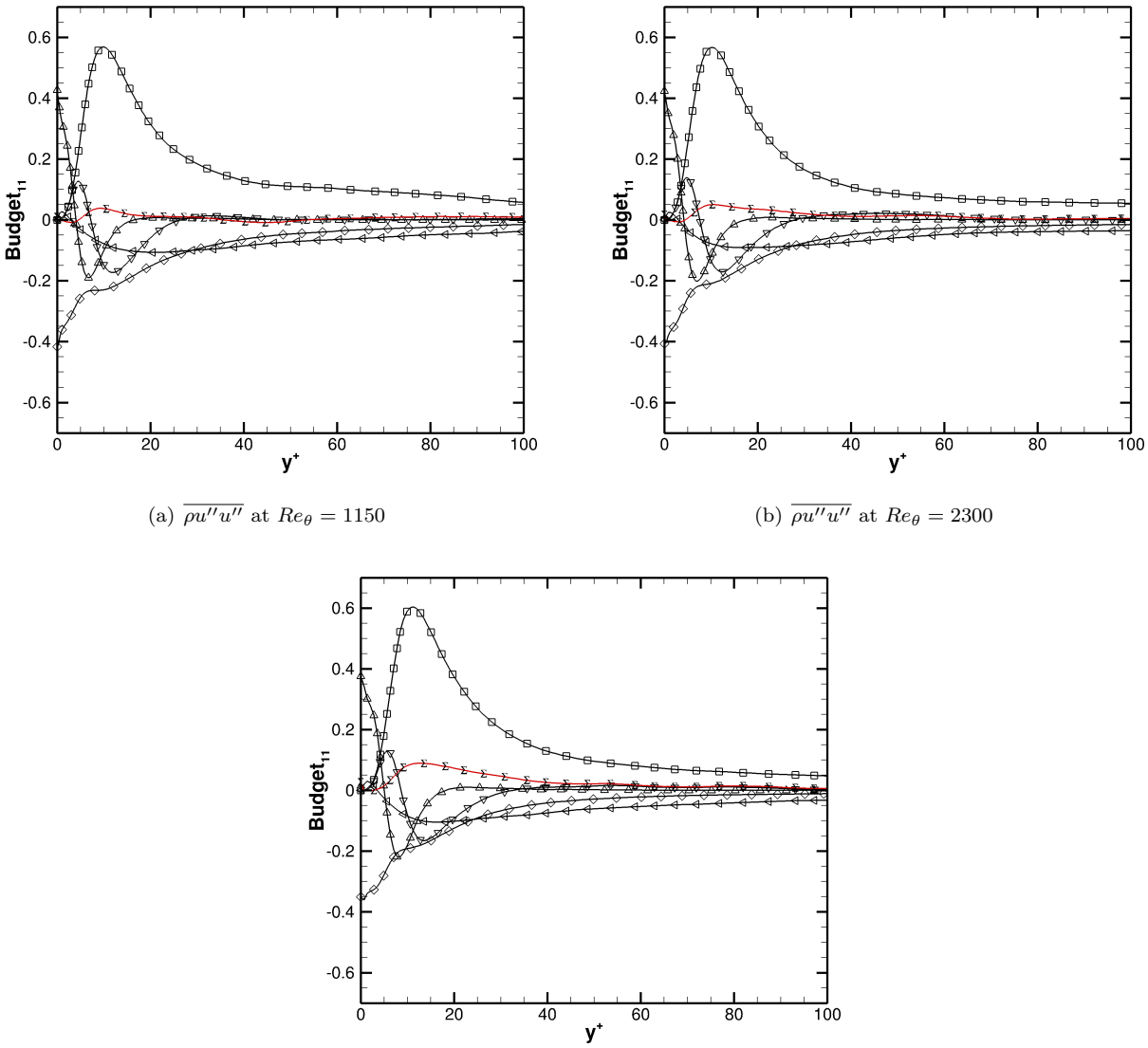

(a) $\overline{\rho u'' u''}$ at $Re_\theta = 1150$

(b) $\overline{\rho u'' u''}$ at $Re_\theta = 2300$

(c) $\overline{\rho u'' u''}$ at $Re_\theta = 4600$

Figure 8. Reynolds-stress budget at $(x - x_{imp})/\delta_{99} = -5.7$ for the coarse mesh. $\overline{\rho u'' u''}$ for present results compared at $Re_\theta = 1150$, 2300, and 4600. □: Production, △: Molecular diffusion, ▽: Turbulent diffusion, ▷: Pressure diffusion, ◁: Pressure strain, ♢: dissipation, ◯: Turbulent mass flux, X: Convection, and Σ: Sum. Terms smaller than three orders of magnitude are omitted from the plots for clarity. Budgets have been normalized by $\rho_w u_\tau^4/\nu_w$.

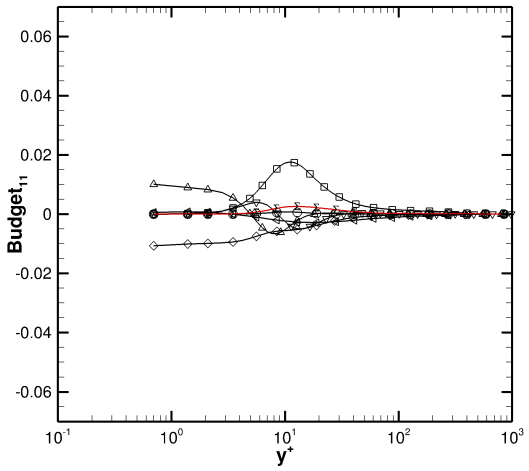

(a) $\overline{\rho u'' u''}$ at $(x - x_{imp})/\delta_{99} = -5.7$

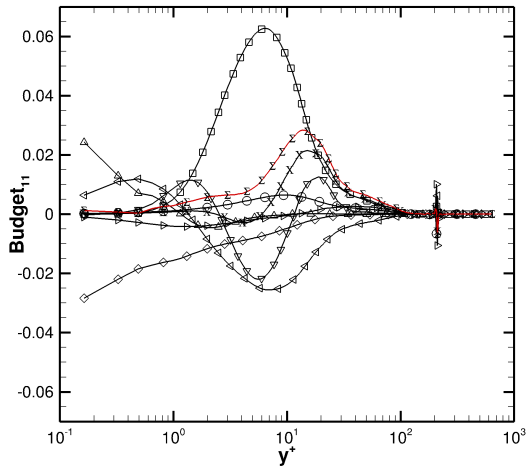

(b) $\overline{\rho u'' u''}$ at $(x - x_{imp})/\delta_{99} = -2.0$

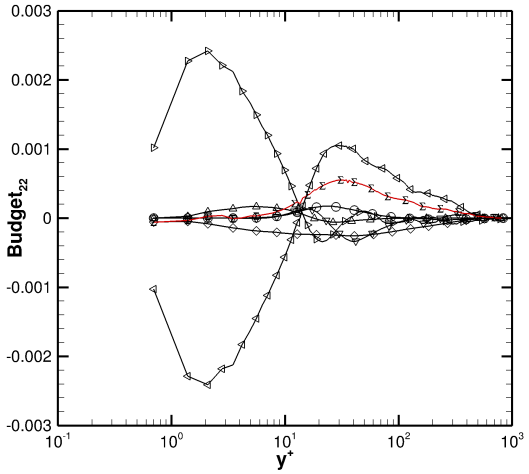

(c) $\overline{\rho v'' v''}$ at $(x - x_{imp})/\delta_{99} = -5.7$

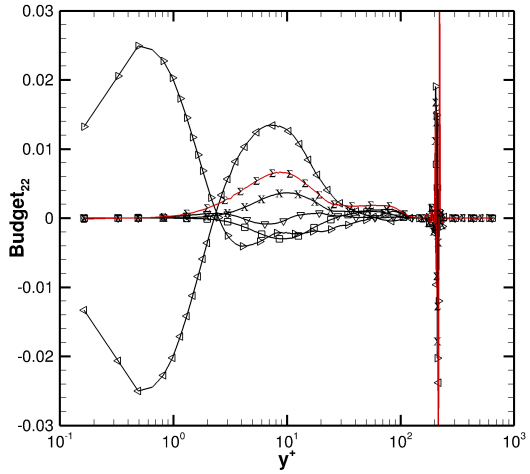

(d) $\overline{\rho v'' v''}$ at $(x - x_{imp})/\delta_{99} = -2.0$

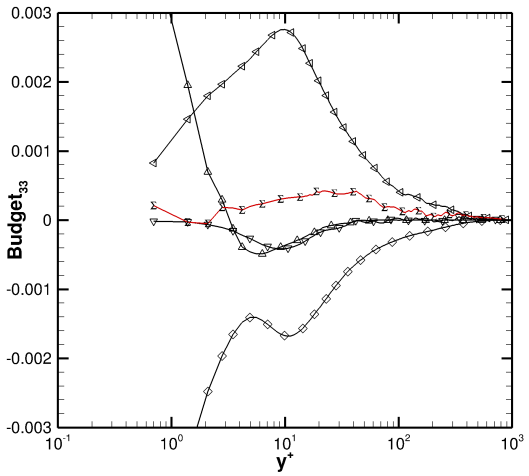

(e) $\overline{\rho w'' w''}$ at $(x - x_{imp})/\delta_{99} = -5.7$

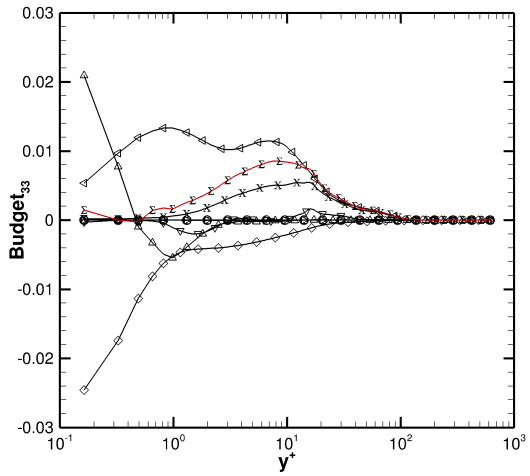

(f) $\overline{\rho w'' w''}$ at $(x - x_{imp})/\delta_{99} = -2.0$

Figure 9. Reynolds normal stress budget for pre-reflected-shock (left panel) and post-reflected-shock (right panel). Coarse mesh at $Re_\theta = 4600$. □: Production, △: Molecular diffusion, ▽: Turbulent diffusion, ▷: Pressure diffusion, ◁: Pressure strain, ♢: dissipation, ◯: Turbulent mass flux, X: Convection, and Σ: Sum. Terms smaller than three orders of magnitude are omitted from the plots for clarity. Budgets are non-dimensionalized by the freestream ($\rho_\infty U_\infty^4/\nu_\infty$), so inner scaling is not applied.

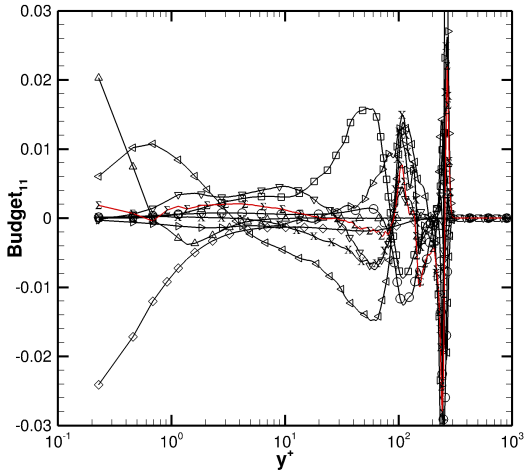

(a) $\overline{\rho u'' u''}$ at $(x - x_{imp})/\delta_{99} = -0.90$

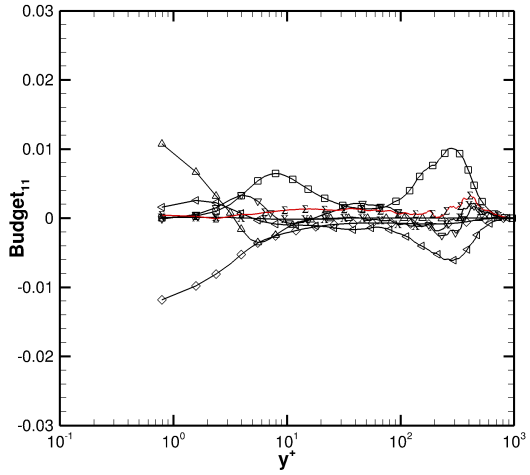

(b) $\overline{\rho u'' u''}$ at $(x - x_{imp})/\delta_{99} = 1.44$

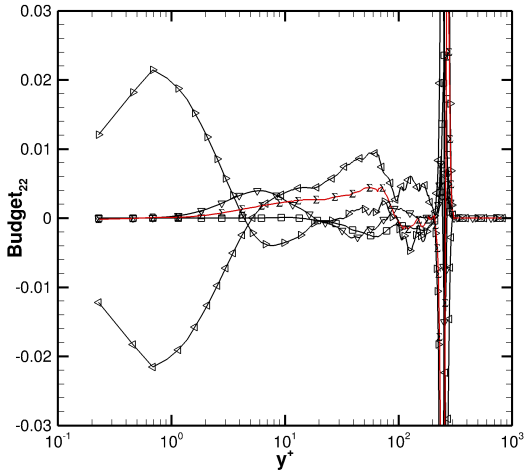

(c) $\overline{\rho v'' v''}$ at $(x - x_{imp})/\delta_{99} = -0.90$

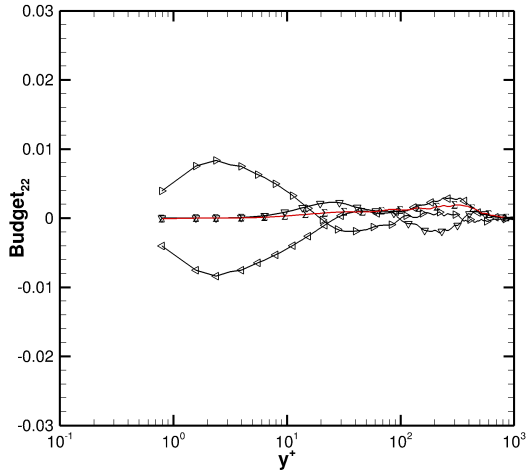

(d) $\overline{\rho v'' v''}$ at $(x - x_{imp})/\delta_{99} = 1.44$

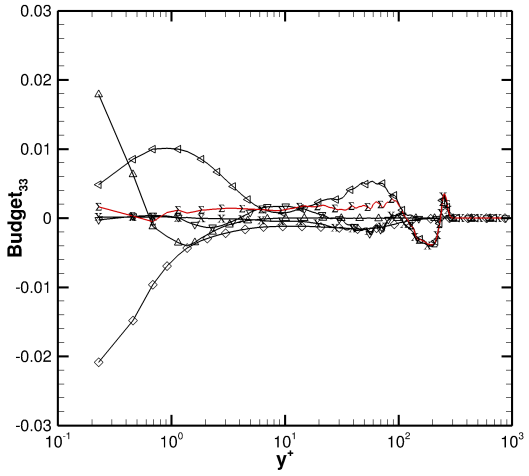

(e) $\overline{\rho w'' w''}$ at $(x - x_{imp})/\delta_{99} = -0.90$

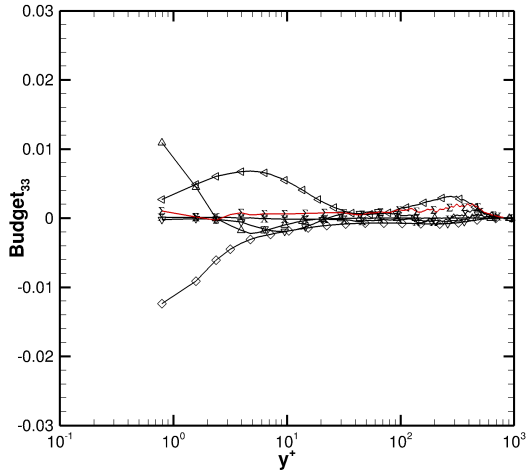

(f) $\overline{\rho w'' w''}$ at $(x - x_{imp})/\delta_{99} = 1.44$

Figure 10. Reynolds normal stress budget for separation (left panel) and post-impinging-shock (right panel). Coarse mesh at $Re_\theta = 4600$. □: Production, △: Molecular diffusion, ▽: Turbulent diffusion, ▷: Pressure diffusion, ◁: Pressure strain, ◊: dissipation, ◯: Turbulent mass flux, X: Convection, and Σ: Sum. Terms smaller than three orders of magnitude are omitted from the plots for clarity. Budgets are non-dimensionalized by the freestream ($\rho_\infty U_\infty^4/\nu_\infty$), so inner scaling is not applied.

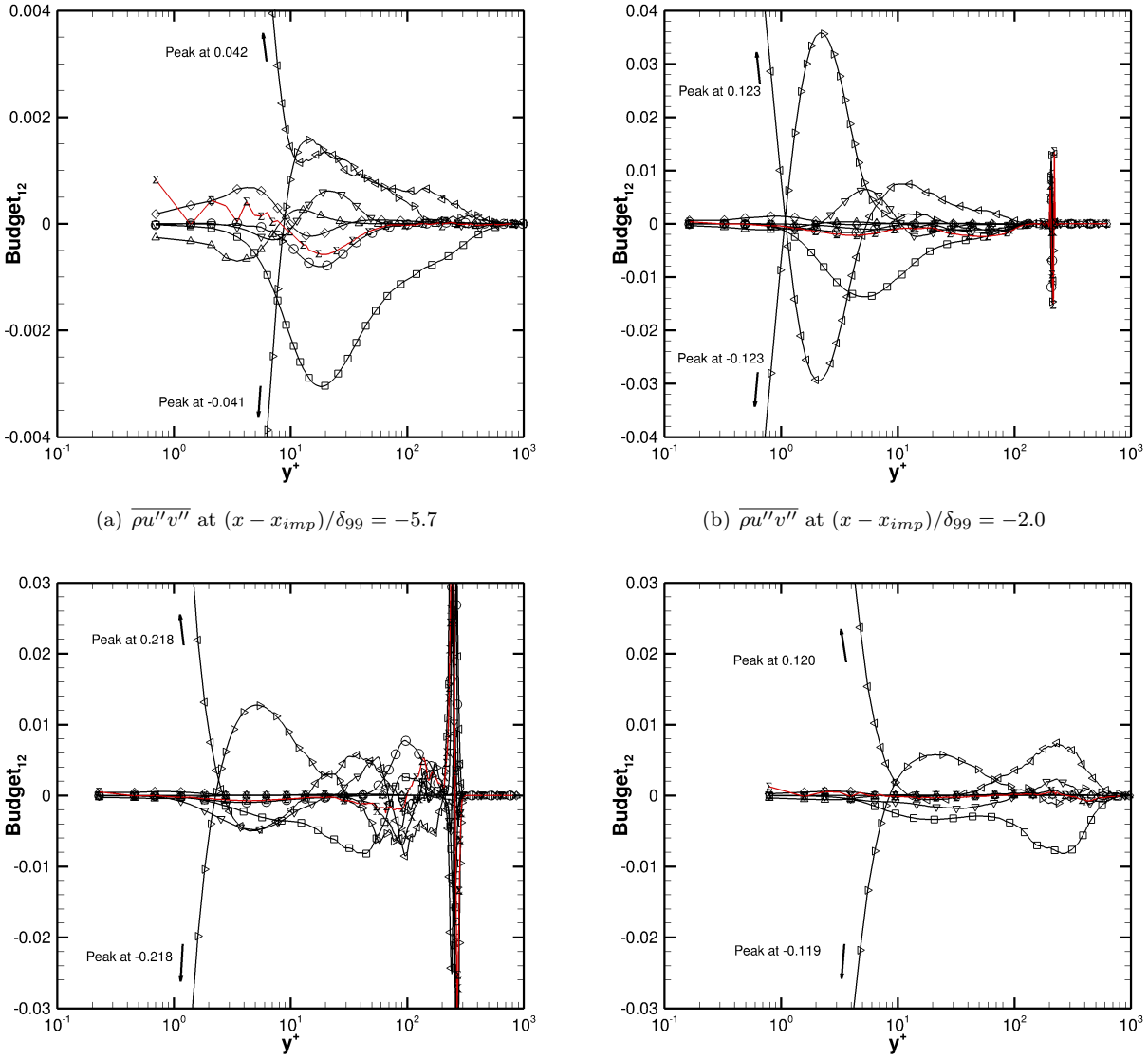

(a) $\overline{\rho u'' v''}$ at $(x - x_{imp})/\delta_{99} = -5.7$

(b) $\overline{\rho u'' v''}$ at $(x - x_{imp})/\delta_{99} = -2.0$

(c) $\overline{\rho u'' v''}$ at $(x - x_{imp})/\delta_{99} = -0.9$

(d) $\overline{\rho u'' v''}$ at $(x - x_{imp})/\delta_{99} = 1.44$

Figure 11. Reynolds shear stress budget for all locations in figures 9 and 10. Coarse mesh at $Re_\theta = 4600$. □: Production, △: Molecular diffusion, ▽: Turbulent diffusion, ▷: Pressure diffusion, ◁: Pressure strain, ♢: dissipation, ◯: Turbulent mass flux, X: Convection, and Σ: Sum. Terms smaller than three orders of magnitude are omitted from the plots for clarity. Budgets are non-dimensionalized by the freestream ($\rho_\infty U_\infty^4/\nu_\infty$), so inner scaling is not applied.